BLACK HOLE MASS DETERMINATION IN THE X-RAY BINARY 4U 1630–47: SCALING OF SPECTRAL AND VARIABILITY CHARACTERISTICS

ELENA SEIFINA[1], LEV TITARCHUK[2,3,4], AND NIKOLAI SHAPOSHNIKOV[4,5]

[1] Moscow M. V. Lomonosov State University/Sternberg Astronomical Institute, Universitetsky Prospect 13, Moscow 119992, Russia; seif@sai.msu.ru
[2] Dipartimento di Fisica, Università di Ferrara, Via Saragat 1, I-44122 Ferrara, Italy; titarchuk@fe.infn.it
[3] George Mason University Fairfax, VA 22030, USA
[4] Goddard Space Flight Center, NASA, Code 663, Greenbelt, MD 20771, USA; lev@milkyway.gsfc.nasa.gov, nikolai.v.shaposhnikov@nasa.gov
[5] CRESST/University of Maryland, Department of Astronomy, College Park, MD 20742, USA
Received 2013 February 27; accepted 2014 May 13; published 2014 June 13

ABSTRACT

We present the results of a comprehensive investigation on the evolution of spectral and timing properties of the Galactic black hole candidate 4U 1630–47 during its spectral transitions. In particular, we show how a scaling of the correlation of the photon index of the Comptonized spectral component Γ with low-frequency quasi-periodic oscillations (QPOs), ν_L, and mass accretion rate, $\dot{M}$, can be applied to the black hole mass and the inclination angle estimates. We analyze the transition episodes observed with the *Rossi X-Ray Timing Explorer* and *BeppoSAX* satellites. We find that the broadband X-ray energy spectra of 4U 1630–47 during all spectral states can be modeled by a combination of a thermal component, a Comptonized component, and a red-skewed iron-line component. We also establish that Γ monotonically increases during transition from the low-hard state to the high-soft state and then saturates for high mass accretion rates. The index saturation levels vary for different transition episodes. Correlations of Γ versus ν_L also show saturation at $\Gamma \sim 3$. Γ–$\dot{M}$ and Γ–ν_L correlations with their index saturation revealed in 4U 1630–47 are similar to those established in a number of other black hole candidates and can be considered as an observational evidence for the presence of a black hole in these sources. The scaling technique, which relies on XTE J1550–564, GRO 1655–40, and H1743–322 as reference sources, allows us to evaluate a black hole mass in 4U 1630–47 yielding $M_{\rm BH} \sim 10 \pm 0.1$ solar masses and to constrain the inclination angle of $i \lesssim 70°$.

Key words: accretion, accretion disks – black hole physics – radiation mechanisms: non-thermal – stars: individual (4U 1630–47)

Online-only material: color figures

1. INTRODUCTION

The problem of the dynamical mass determination of black holes (BHs) in binary systems is closely related to mass function and mass ratio estimates (using optical counterpart data) and also to the orbital inclination angle (see Orosz 2003, and references therein). This mass determination requires a knowledge of the period and radial velocity measurement. The absence of X-ray eclipses and the rotational broadening of absorption lines (radial velocity shifts) in the optical star spectrum also facilitate BH mass evaluation. However, there are relatively few low-mass binary sources for which optical emission is accessible, as a result of Galactic extinction. On the other hand, it is possible to evaluate the mass of the central object (for example, a BH mass) based on X-ray data and timing characteristics (even when conventional dynamical methods cannot be used). Furthermore, only in transient systems where accretion shuts down and the system reverts to a quiescent state can the Keplerian photospheric line shifts be measured.

A new method of the BH mass determination was developed by Shaposhnikov & Titarchuk (2009), hereafter ST09, using correlation scaling between X-ray spectral and timing properties observed from many Galactic BH binaries during their hard-soft state transitions. ST09 consider the transition layer (TL) model proposed by Titarchuk et al. (1998), hereafter TLM98 (see also Titarchuk & Osherovich 1999, hereafter TO99), in which the TL size is proportional to BH mass. The Comptonization parameter Y, which is a product of the average number of scatterings and the efficiency of upscattering, is inversely proportional to the energy spectral index α (ST09). TLM98 suggest that such a configuration is a result of an adjustment of a Keplerian flow

(disk) to a turbulent, innermost sub-Keplerian flow (TL). The TL formation is probably related to the shock formation near the adjustment radius (see TLM98). Thus, the accretion flow releases its gravitational energy in the TL where its temperature is regulated by this gravitational energy release, Compton cooling, and illumination of the TL by external soft photon flux from the disk (see TLM98 and TO99). The emergent spectrum is formed as a result of upscattering of these soft (disk) photons in the relatively hot plasma of the TL. In the low-hard state, when the flux of the disk photons is relatively weak, the TL plasma temperature is $kT_e \sim 50$ keV and the resulting photon index is $\Gamma \lesssim 1.9$. On the other hand, in the high-soft state, when the flux of the disk soft photon dominates the gravitational energy release in the TL, the plasma temperature significantly decreases to 5–10 keV and the photon index Γ becomes greater than 2 as a result of disk photon cooling and general relativity (GR) effects (see Titarchuk & Zannias 1998; Laurent & Titarchuk 1999).

It is well known that different black hole candidates (BHCs) show different spectral-timing correlation patterns, Γ versus quasi-periodic oscillation (QPO) frequency ν_L and Γ versus mass accretion rate, depending on mass of the compact object, the distance from the Earth observer, and the binary inclination. The correlation of Γ versus ν_L in black hole binaries was discovered by Vignarca et al. (2003) using *Rossi X-Ray Timing Explorer* (*RXTE*) data in terms of a phenomenological model, a high-energy cutoff power law, corrected for interstellar absorption, plus a Gaussian emission line to take into account an excess at 6.4 keV. Recently Stiele et al. (2013, hereafter SBKM13) confirmed the correlations between the spectral index and QPO frequency in a sample of Galactic BHC binaries (GX 339–4, H1743–322, and XTE J1650–500) using *RXTE* data. For the

spectral fitting they applied a sum of the disk emission approximated by the *diskbb* model (Mitsuda et al. 1984) with the *simpl* model (Steiner et al. 2009) for Compton scattering as well as a reflection component. However, Vignarca et al. and Stiele et al. did not apply these induced correlations for BH mass determination.

In the studies of Shaposhnikov & Titarchuk (2007, 2009, hereafter ST07), Titarchuk & Seifina (2009, hereafter TS09), and Shrader et al. (2010), the authors demonstrate that these correlation tracks provide a wide scaling range for a source with unknown BH mass. Recently, application of this method was also extended to a study of another class of X-ray sources, the ultraluminous X-ray source (ULX) NGC 5408 X-1 in Strohmayer & Mushotzky (2009). Moreover Giacchè et al. (2014), hereafter GGT14 applied a scaling technique based on the observed correlation to estimate the BH mass in the narrow-line Seyfert 1 galaxy Mrk 766. This technique is the first time it has been applied in detail to estimate the BH mass, M_{BH} in an AGN. GGT14 obtained a value of $M_{BH} = 1.26^{+1.00}_{-0.77} \times 10^6\, M_\odot$, which is in very good agreement with that estimated by the reverberation mapping.

The observed variability and spectral properties vary in a well-defined manner throughout different spectral states. Furthermore, these correlations are seen in many sources, which vary widely in luminosity. The universality of these correlations suggests that the basic physical processes are very similar for each of these sources and their observational manifestations are determined by a common set of basic physical parameters.

In this work we take an opportunity to determine the mass of the putative BH in the X-ray binary 4U 1630–47, for which the compact object mass has not been evaluated using any traditional method (see above). 4U 1630–47 is an X-ray transient discovered by *Uhuru* (see Jones et al. 1976), although its first recorded outburst was apparently detected in 1969 by *Vela-5B* (Priedhorsky 1986). 4U 1630–47 is a well-studied BHC (Tanaka & Lewin 1995; Parmar et al. 1995, 1997; Kuulkers et al. 1997; Oosterbroek et al. 1998). 4U 1630–47 is an ultra-soft X-ray transient, which shows various multiple outbursts. 4U 1630–47 has also been observed by *Ginga* (Kuulkers et al. 1997), *BeppoSAX* (Oosterbroek et al. 1998), *International Gamma-Ray Astrophysics Laboratory* (*INTEGRAL*; Tomsick et al. (2005), hereafter T05), and *Suzaku* (Kubota et al. 2007). The 1984 outburst and its following decay were studied by *EXOSAT* (Parmar et al. 1986). 4U 1630–47 is a part of the group of X-ray transients known as X-ray novae (Tanaka & Shibazaki 1996; Sunyaev et al. 1994). All sources of this type are assumed to be recurrent. However, the recurrence timescales seem to range from years to decades, so in some cases only a single event has been recorded (e.g., Chen et al. 1997; Grindlay et al. 2014). A typical recurrence time for outbursts of such sources is usually ∼10–50 yr. In this respect, the fact that 4U 1630–47 and also GX 339–4 exhibit relatively frequent outbursts is uncommon. The source 4U 1630–47 lies in the direction toward the Galactic center. Observations show that the source is heavily absorbed in soft X-rays, indicating a large source distance (⩾10 kpc). No optical counterpart has yet been identified, probably due to the large extinction amount of optical (>20 mag) and reddening. Therefore, the dynamical evidence for the presence of a black hole (BH) in this binary system is still missing.

For the reasons mentioned above the binary orbital period of 4U 1630–47 is not known. The spread in estimates of the column density toward 4U 1630 is quite broad. Specifically, N_H values as derived from spectral fits of X-ray data are in the range from 5×10^{22} cm^{-2} (Parmar et al. 1986, 1997) to 1.5×10^{23} cm^{-2} (Kuulkers et al. 1998; T05; Oosterbroek et al. 1998; Cui et al. 2000; Dieters et al. 2000; Tomsick & Kaaret 2000; Trudolyubov et al. 2001). These measurements vary with X-ray brightness of the system and clearly include a contribution intrinsic to the system. The column density estimate derived from H I radio surveys (Kerr et al. 1986) yields a value of 2×10^{22} cm^{-2}. Some difficulties of the infrared counterpart detection of this X-ray source are related to the requirement of continuous and deep IR monitoring during both outburst and quiescence (Callanan et al. 2000). Augusteijn et al. (2001) were able to detect a variable source at $K = 16.1$ mag located inside the radio error circle, which they identify as the infrared counterpart to the X-ray source. They conclude that 4U 1630–47 is most likely a BHC X-ray binary similar to GRO J1655–40 or 4U 1543–47, containing a relatively early-type secondary. It should be noted that among multiple X-ray outbursts registered from 4U 1630–47, only the 1998 outburst was accompanied by radio jet emission (Hjellming et al. 1999) detected by NRAO Very Large Array (VLA) and Australia Telescope Compact Array (ATCA). Based on its similarities to the X-ray properties of sources in which a BH has been identified using the dynamical methods, 4U 1630–47 is also suggested to be a BHC (see, e.g., Parmar et al. 1986).

The emission properties of accreting BHs are generally classified in terms of *canonical* "spectral states" (see Remillard & McClintock 2006; Belloni et al. 2005; Klein-Wolt & van der Klis 2008). We use a general BH state classification that includes five basic BH states: *quiescent*, *low-hard*, *intermediate*, *high-soft*, and *very high states* (LHS, IS, HSS, and VHS, respectively). When a BH goes into outburst, it starts from its *quiescent* state and enters the LHS, where the energy spectrum is characterized by a hard Comptonization component and a relatively weak thermal component. This spectrum is a result of Comptonization of soft photons by electrons of the hot ambient media [the Compton cloud, herein CC] (see, e.g., Sunyaev & Titarchuk 1980). Throughout this work we use terminology where the CC is associated with a TL. In general, the LHS is characterized by strong variability, which can been seen as a flat-top broken power law (WRN) in its power density spectrum (PDS), along with QPOs in the range of 0.01–25 Hz.

In the HSS, the photon spectrum is well represented by the sum of a strong thermal component, which probably originated in the inner accretion disk, and an extended power-law component. It is worth noting that in the HSS the PDS flat-top component is absent and all QPOs disappear. Overall variability in the HSS is either absent or very low and presented by a weak power law in the power spectrum. The intermediate state (IS) is a transitional state from the LHS to the HSS and vice versa. Note that in addition to the LHS, IS, and HSS we can also observe sometimes a very high state (VHS) in which both *blackbody* and non-thermal components are present. Flat-top noise and low-frequency QPOs (LFQPOs) may be seen in their PDSs. Also, this state is generally associated with high-frequency QPOs above 100 Hz.

Three main types of LFQPOs, so-called Type A, B, and C, were originally identified in the light curve of XTE J1550–564 (Wijnands et al. 1999; Remillard et al. 2002) and later found in several other sources (see Casella et al. 2005, and references therein). In the context of the state classification outlined above, it is possible to attribute these three QPO types to different spectral conditions (see Homan et al. 2001; Homan & Belloni 2005; Belloni et al. 2005). The C-type QPO is associated with

Table 1
BeppoSAX Observations of 4U 1630–47 used in Analysis

N	Obs. ID	Start Time (UT)	End Time (UT)	MJD Interval
S1	20114001	1998 Feb 20 04:30:02	1998 Feb 20 16:55:45	50864.2–50864.7[1]
S2	20114002	1998 Feb 24 05:32:00	1998 Feb 24 15:00:40	50868.2–50868.6[1]
S3	20114003	1998 Mar 7 12:23:21	1998 Mar 8 03:52:21	50879.5–50880.1[1]
S4	20114004	1998 Mar 19 14:52:11	1998 Mar 20 04:18:08	50891.6–50892.3[1]
S5	20114005	1998 Mar 26 17:16:48	1998 Mar 27 09:59:27	50898.7–50899.4[1]
S6	70566001	1998 Aug 6 18:10:26	1998 Aug 7 17:59:20	51031.7–51031.3[2]
S7	70821005	1999 Aug 8 19:26:53	1998 Aug 10 17:33:02	51398.8–51400.1[2]

References. (1) Oosterbroek et al. 1998; (2) Dieters et al. 2000.

the (radio-loud) hard intermediate state and the low/hard (LS) state (Soleri et al. 2008). It is commonly seen in almost all BHCs in which a QPO is correlated with the count rate and this QPO is characterized by a high fractional variability. In turn, C-type QPOs demonstrate a clear correlation with the spectral index and provide an opportunity for a BH mass scaling (ST07, ST09). Casella et al. (2005) showed that the QPO type and frequency in BHCs change systematically as a function of the inverse of the source rms fractional variation. This behavior is seen over different BHCs and presents fair similarities with the LFQPOs observed in neutron star (NS) low-mass X-ray binaries. Thus, Casella et al. (2005) suggested that C-, B-, and A-type LFQPOs in BHCs correspond to horizontal, normal, and flaring branch oscillations (HBOs, NBOs, and FBOs, respectively) of high-luminosity NS systems of the Z class.

Based on the analysis of *RXTE* data, T05 concluded that 4U 1630–47 exhibits many properties that are not completely encompassed by Remillard & McClintock (2006) state definitions. In particular, T05 reported on a so-called *flaring* state observed on timescales of 10–100 s during 2002–2004 observations. Similar high-amplitude flaring behavior was previously detected only in BHC GRS 1915+105 (Belloni et al. 2005). However, in contrast to the GRS 1915+105 case, the X-ray light curves of 4U 1630–47 do not show the repeating patterns seen in GRS 1915+105.

In this work we study in detail the behavior of the energy and power spectra observed by *RXTE* and *BeppoSAX* from the galactic BHC 4U 1630–47 during 1996–2004 outburst activity. Specifically, we concentrate on the phenomenology of the photon index and the QPO frequency. Based on the results of our data analysis, we estimate the BH mass in 4U 1630–47. In Section 2 we present the list of observations used in the data analysis, while in Section 3 we provide the details of X-ray spectral analysis. We discuss the evolution of X-ray spectral and timing properties during the state transition in Sections 4–6. We also discuss our results and make our final conclusions in Sections 7 and 8.

2. DATA SELECTION

Broadband energy spectra of 4U 1630–47 were obtained combining data from three *BeppoSAX* Narrow Field Instruments (NFIs): the Low Energy Concentrator Spectrometer (LECS; Parmar et al. 1997) for the 0.3–4 keV range, the Medium Energy Concentrator Spectrometer (MECS; Boella et al. 1997) for the 1.8–10 keV range, and the Phoswich Detection System (Frontera et al. 1997) for the 15–200 keV range. The SAXDAS data analysis package is used for the data processing. We performed spectral analysis for each instrument in a corresponding energy range with a well-known response matrix. The LECS data

have been renormalized to match the MECS data. Relative normalizations of the NFIs were treated as free parameters in the model fits, except for the MECS normalization that was fixed at unity. The cross-calibration factor obtained in this way is found to be in a standard range for each instrument.[6] Additionally, spectra have been rebinned in accordance with the energy resolution of the instruments using rebinning template files in GRPPHA to obtain better signal-to-noise ratioSystematic uncertainties of 1% have been applied to all spectra. In Table 1 we listed the *BeppoSAX* observations used in the present analysis.

We also analyzed 425 *RXTE* observations taken between 1996 February and 2004 May. Standard tasks of the LHEASOFT/ FTOOLS 5.3 software package were used for data processing. For spectral analysis we used PCA *Standard 2* mode data, collected in the 3–23 keV energy range, applying PCA response calibration (pcarmf v11.7). The fitting was carried out using the standard XSPEC v 12.6.0 fitting package.[7] The standard dead-time correction procedure has been applied to the data. In order to construct broadband spectra, the data from HEXTE detectors have been also utilized. We subtracted a background corrected in off-source observations. The data are available through the GSFC public archive (http://heasarc.gsfc.nasa.gov). A systematic error of 0.5% has been applied to all analyzed *RXTE* spectra. In Table 2 we listed the groups of *RXTE* observations tracing thorough the source evolution during different states.

We have performed an analysis of *RXTE* observations of 4U 1630–47 spanning eight years made at seven intervals indicated by blue rectangles in Figure 1 (top). The *RXTE* energy spectra were modeled using XSPEC astrophysical fitting software. We have also used public 4U 1630–47 data from the All-Sky Monitor (ASM) on board *RXTE*, which demonstrate long-term variability of the 2–12 keV flux during all observation scans.

According to ASM monitoring, 4U 1630–47 shows complex long-term variations. Specifically, during eight years (1996–2004) *RXTE* has detected five outbursts from 4U 1630–47 (see Figure 1). These outbursts follow the recurrence interval of about 600 days (Parmar et al. 1995) and differ significantly in shape.

Possible resemblance between individual outbursts from 4U 1630–47 and from other known BHCs should be emphasized. For example, the outbursts of 1996 and 1999 resemble the state transitions in the persistent BHC Cyg X-1 (Cui et al. 1998) and GX 339–4 (Belloni et al. 1999), while the 1998 outburst showed a fast rise and exponential decay (FRED) profile, which is typical for many X-ray novae (Chen et al. 1997).

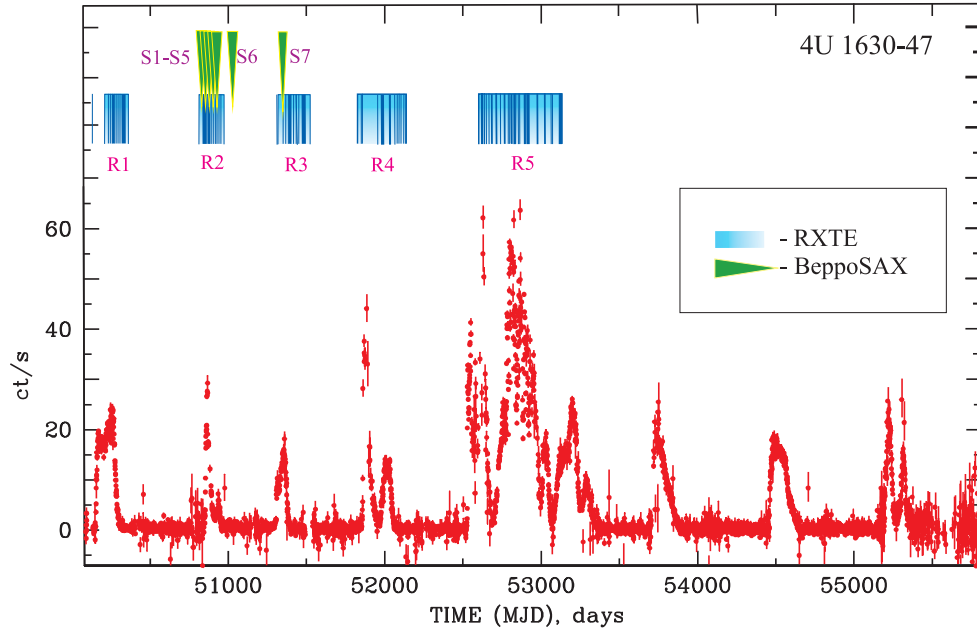
[6] http://heasarc.nasa.gov/docs/sax/abc/saxabc/saxabc.html
[7] http://heasarc.gsfc.nasa.gov/FTP/sax/cal/responses/grouping

Figure 1. Evolution of ASM/*RXTE* count rate during 1996–2011 observations of 4U 1630–47. Blue vertical strips (at top of the panel) indicate temporal distribution of the *RXTE* data of pointed observations used in our analysis, whereas bright blue rectangles indicate the *RXTE* data sets listed in Table 2, and green triangles show *BeppoSAX* NFI data, listed in Table 1.

(A color version of this figure is available in the online journal.)

Table 2
RXTE Observations of 4U 1630–472

Number of Set	Dates, MJD	RXTE Proposal ID	Dates UT	Rem.	Ref.
R1	50114	00033	1996 Feb 1		
	50206−50311	10411	1996 May 3–Aug 16		1, 2, 3
R2	50876−50972	30172	1998 Mar 4–Jun 8	*BeppoSAX*	4, 5
	50853−50903	30178	1998 Mar 9–Mar 31	*BeppoSAX*	4, 6
	50855−50873	30188	1998 Feb 11–Mar 1	*BeppoSAX*	4, 6
	50988−50990	30410	1998 Jun 24–Jun 26		
R3	51537−51557	40112	1999 Dec 25–2000 Jan 14		
	51306−51405	40418	1999 May 8–Sep 15	*BeppoSAX*	
R4	51864−51914	50120	2000 Nov 16–2001 Jan 5		
	51917−51978	50135	2001 Jan 8–March 10		
	51980−52077	60118	2001 Mar 12–Jun 17		
R5	52519−52654	70417	2002 Sep 12–2003 Jan 16		7, 8
	52658−52689	70113	2003 Jan 19–Feb 19		7
	52790−53081	80117	2003 May 31–2004 May 17		7

References. (1) Marshall 1996; (2) Levine et al. 1996; (3) Kuulkers et al. 1998; (4) Trudolyubov et al. 2001; (5) Tomsick & Kaaret 2000; (6) Dieters et al. 2000; (7) Tomsick et al. 2005; (8) Homan & Wijnands 2002.

Data from the PCA and HEXTE detectors, as well as *BeppoSAX* detectors, have been used to constrain spectral fits, while ASM data provided long-term intensity state monitoring. Results of our long-term study of 4U 1630–47 are presented in detail in the next sections and compared with results for XTE J1550–564 in order to estimate a BH mass in 4U 1630–47.

In general, the broadband spectral sensitivities of two X-ray orbital observatories, *RXTE* (Bradt et al. 1993) and *BeppoSAX* (Boella et al. 1997), combined with the high timing resolution of *RXTE*, provide a means to study both the detailed broadband spectra and long-term spectral and timing evolution of BH-hosting X-ray binaries.

3. SPECTRAL ANALYSIS

Our spectral model is based on the following physical paradigm of the accretion process. We assume that accretion

onto a BH takes place when the material passing through three main regions—a geometrically thin accretion disk (standard Shakura-Sunyaev disk; see Shakura & Sunyaev 1973), the TL (Titarchuk et al. 1998), and the converging flow—(Titarchuk & Zannias 1998). The disk photons are upscattered off energetic electrons of the TL and the converging flow (see also Figure 2). Some fraction of these seed photons can be also seen directly by the Earth observer. *Pink* and *blue* waved arrows shown in Figure 2 correspond to *Comptb* and blackbody components, respectively.

According to the physical picture described above, for our spectral analysis we use a model that consists of the sum of a Comptonization (*Comptb*) component, (*COMPTB* is the XSPEC Contributed model;[8] see Farinelli et al. 2008), a

_____

[8] http://heasarc.gsfc.nasa.gov/docs/software/lheasoft/xanadu/xspec/models/comptb.html
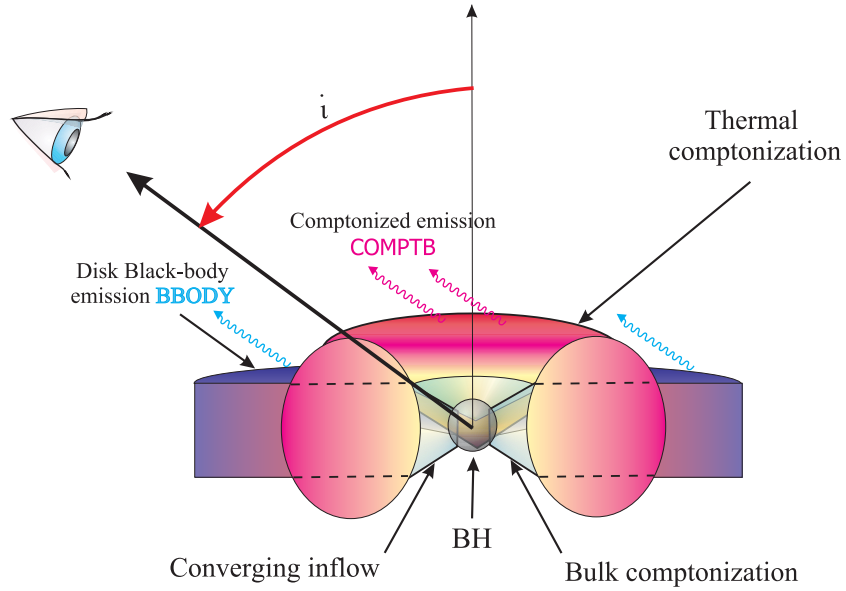
Figure 2. Suggested geometry of the system. Disk soft photons are upscattered (Comptonized) off relatively hot plasma of the transition layer. Some fraction of these photons are directly seen by the Earth observer. Blue and pink photon trajectories correspond to soft (disk) and hard (Comptonized) photons, respectively.

(A color version of this figure is available in the online journal.)

soft *Blackbody* component, and the iron-line component. The *Comptb* spectral component has the following parameters: temperature of the seed photons T_s, energy index of the Comptonization spectrum α $(= \Gamma - 1)$, electron temperature kT_e, Comptonization fraction f [$f = A/(1 + A)$], and normalization of the seed photon spectrum $N_{\rm com}$.

Some observations show that significant excess of emission in the 6–8 keV region occurs, which one can attribute to the iron emission complex. The presence of the iron-linefeatures provides the evidence for an additional *reprocessed* component in the spectrum. It should be noted that a subset of observations can be fit without adding the iron line (∼30%), while the remaining observations require the line component including either two narrow iron K_α emission lines (*Gaussians*) or one red-skewed iron K_α emission line (modeled by the *Laor* XSPEC model). Model fits for several spectra show that the *Laor*-line component is more suitable than the sum of two *Gaussians*. For these reasons, an iron K_α-line (*Laor*) component (Laor 1991) was included in our model spectrum and applied to all spectra. The *Laor* model parameters are the line energy, E_L, the emissivity index, a dimensionless inner disk radius, $r_{\rm in} = R_{\rm in}/R_g$ (with $R_g = GM_{\rm BH}/c^2$), inclination, i, and the normalization of the line, N_L (in units of photons cm^{-2} s^{-1}). Note that R_g is the gravitational radius of a BH, with G and c as the common physical constants and $M_{\rm BH}$ as a BH mass. For the *Laor* component we fixed the outer disk radius to the default value of 400 R_g, while we vary all the parameters allowed to be free. We also fixed the emissivity index to 3. The inclination is constrained to a value $i \sim 70°$, which is estimated using the scaling technique (see Section 7.3).

In turn, to fit the data in the 1–4 keV range, we use a *blackbody* component for which parameters are the normalization N_{BB} and color temperature kT_{BB}. In the model we also include interstellar absorption with a column density $N_{\rm H}$.

During the fitting procedure, we fix certain parameters of the *Comptb* component. First, we put $\gamma = 3$. Note that the low energy index of the seed blackbody spectrum is $\gamma - 1 = 2$. We also fixed the value of the *Comptb* parameter $\log(A)$ to 2 when the best-fit values of $\log(A) \gg 1$ a Comptonization

fraction $f = A/(1 + A)$ equals approximately to 1 and the model fit becomes insensitive to the parameter. We use a value of the hydrogen column density $N_{\rm H} = 7.7 \times 10^{22}$ cm^{-2}, which was found by Dieters et al. (2000). As a result, we obtain a satisfactory agreement with this model for both *RXTE* and *BeppoSAX* for all available observations.

We show examples of fits of X-ray spectra using our spectral model in Figures 3 and 4 (for *BeppoSAX* data) and in Figures 5 and 6 (for *RXTE* data). Spectral analysis of *BeppoSAX* and *RXTE* observations indicates that X-ray spectra of 4U 1630–47 can be satisfactory fit by the model where its Comptonization component is present by the *Comptb* model. Moreover, for the broadband *BeppoSAX* observations this spectral model component allows us to describe the photoelectric absorption at low energies ($E < 3$ keV) and the structure of Fe K band over 6–7 keV energy band in detail.

3.1. BeppoSAX Data Analysis

In Figure 3 we demonstrate three representative EF_E spectral diagrams (green lines) for different states of 4U 1630–47. Data are taken from *BeppoSAX* observations 20114002 (left panel, "S2" data set, HSS), 20114005 (central panel, "S5" data set, IS), and 70821005 (right panel, "S7" data set, LHS). The data are shown by black crosses, and the spectral model components are displayed by dashed red, blue, and purple lines for the *Comptb*, *Blackbody*, and *Laor*, respectively. Yellow shaded areas demonstrate an evolution of the *Comptb* component during the state transition between the HSS (S2) and LHS (S7) when the normalization parameter $N_{\rm com}$ of the Comptonization component monotonically decreases from 13 to $2 \times L_{37}/d_{10}^2$ erg s^{-1} kpc^{-2}. In the bottom panels we show the corresponding $\Delta\chi$ versus photon energy (in keV).

The best-fit model parameters for the HSS state (left panel, S2) are $\Gamma = 2.62 \pm 0.05$, $kT_e > 230$ keV, and $E_{\rm line} = 6.42 \pm 0.04$ keV [$\chi^2_{\rm red} = 1.16$ for 127 degrees of freedom (dof)], while the best-fit model parameters for the IS state (central panel, S5) are $\Gamma = 2.03 \pm 0.03$, $kT_e = 58 \pm 1$ keV, and $E_{\rm line} = 7.08 \pm 0.06$ keV [$\chi^2_{\rm red} = 1.18$ for 127 dof]; and, finally, the
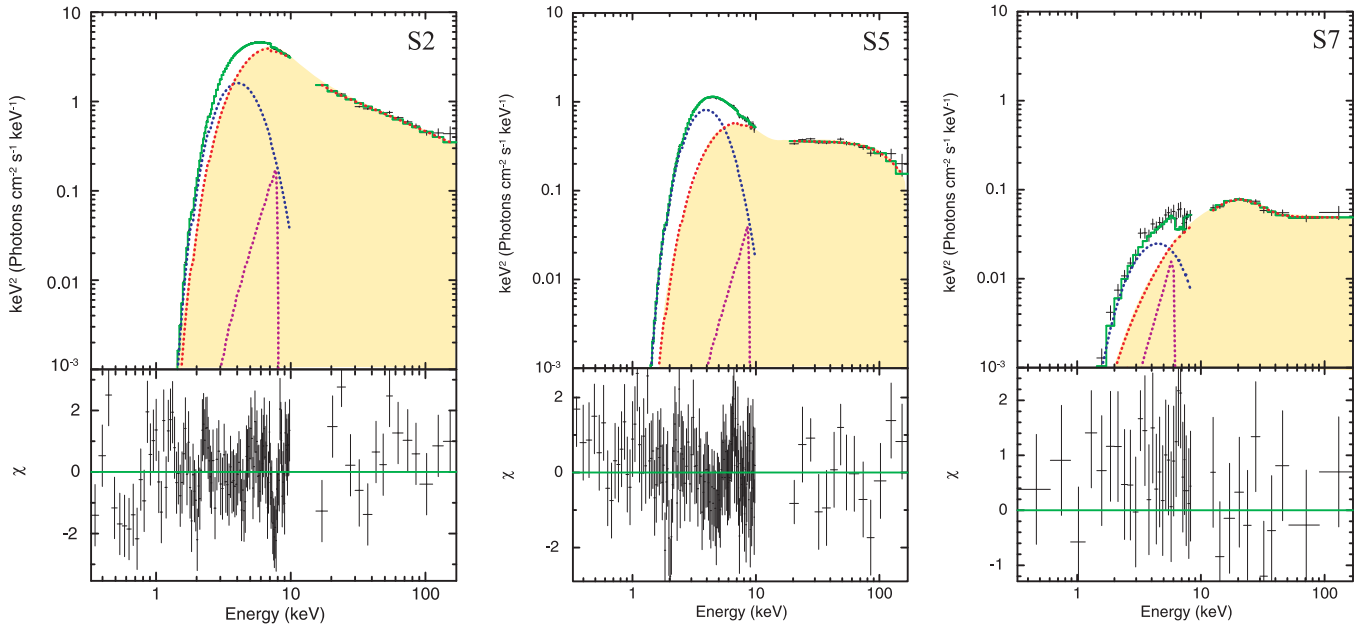
Figure 3. Three representative EF_E diagrams for different states of 4U 1630–47 (green lines). Data are taken from *BeppoSAX* observations 20114002 (left panel, "S2" data set, HSS), 20114005 (central panel, "S5" data set, IS), and 70821005 (right panel, "S7" data set, LHS). The data are shown by black crosses, and the spectral model components are displayed by dashed red, blue, and purple lines for *Comptb*, *Blackbody*, and *Laor*, respectively. Yellow shaded areas demonstrate an evolution of the *Comptb* component during transitions between the HSS (S2) and LHS (S7) when the normalization parameter $N_{\rm com}$ of the Comptonization component monotonically decreases from 13 to 0.5 × L_{37}/d_{10}^2 erg s^{-1} kpc^{-2} (see also Figure 11).

(A color version of this figure is available in the online journal.)
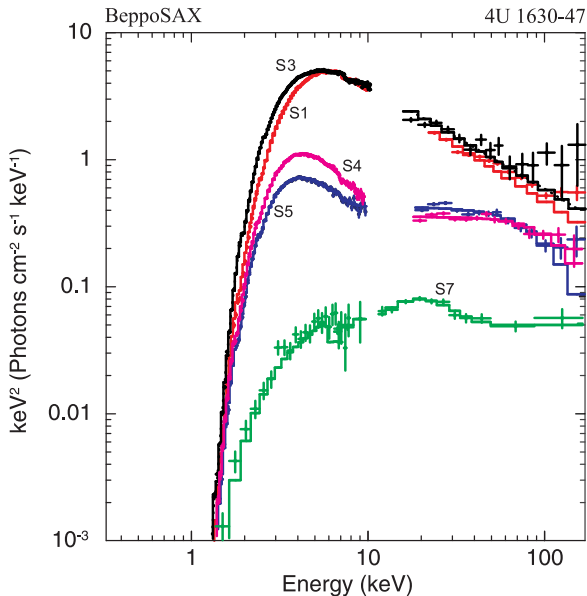

Figure 4. Five representative EF_E spectral diagrams for different states of 4U 1630–47. Data are taken from *BeppoSAX* observations 20114001 (red), 20114003 (black, HSS), 20114004 (pink), 20114005 (blue, IS), and 70821005 (green, LHS).

(A color version of this figure is available in the online journal.)

best-fit model parameters for the LHS state (right panel, *S*7) are $\Gamma = 2.01 \pm 0.02$, $kT_e = 160 \pm 50$ keV, and $E_{\rm line} = 5.38 \pm 0.05$ keV [$\chi^2_{\rm ref} = 0.92$ for 127 dof].

The *blackbody* temperature kT_{BB} weakly depends on the source state and is consistent with 0.7 keV (at a 2-σ level of confidence). Adding this low-temperature *blackbody* component significantly improves the fit quality for the *BeppoSAX* spectra. For example, the best fit for the LHS events (ID = 70821005)

is characterized by reduced $\chi^2_{\rm red}$ of 3.7 (129 dof) for the model *without this low-temperature blackbody component*, while $\chi^2_{\rm red}$ is 0.92 (127 dof) for the model *with the low-temperature blackbody component*. We also find that the seed temperatures kT_s of the *Comptb* component vary only slightly around 1.6 keV. A systematic uncertainty of 1% has been applied to all analyzed *BeppoSAX* spectra (see more details in Table 3).

The general picture of the LHS-IS-HSS transition is illustrated in Figure 4, where we put together spectra of the LHS, IS, and HSS, to demonstrate the source spectral evolution from the high-soft to low-hard states based on the *BeppoSAX* observations. We should point out the fact that the HSS and IS spectra are characterized by a strong soft *blackbody* component and a power law extending up to 200 keV, while in the LHS spectrum, the Comptonization component is dominant and the *blackbody* component is barely seen.

For the *BeppoSAX* data (see Tables 1 and 3) we find that the spectral index α monotonically increases from 1 to 1.7 (or the photon index Γ from 2 to 2.7), when the normalization of the *Comptb* component (or mass accretion rate) changes by a factor of 8.

3.2. RXTE Data Analysis

For the *RXTE* data analysis we use the information that we obtain using the *BeppoSAX* best-fit spectra. Specifically, because *RXTE*/PCA detectors cover energies above 3 keV, for our analysis of *RXTE* spectra we fix a key parameter of the *blackbody* component (kT_{BB} =0.7 keV) obtained as a mean value of kT_{BB} for the *BeppoSAX* spectra. In Figure 5 we show representative spectra of 4U 1630–47 for the LHS, IS, HSS, and VSS. Data are taken from *RXTE* observations 30172-01-18-12 ($\Gamma = 1.6$, LHS), 30172-01-04-00 ($\Gamma = 2.2$, IS), 80117-01-05-00 ($\Gamma = 3.0$, VHS), and 10411-01-03-00 ($\Gamma = 2.0$, HSS). Here data are denoted by black points with error bars. The spectral
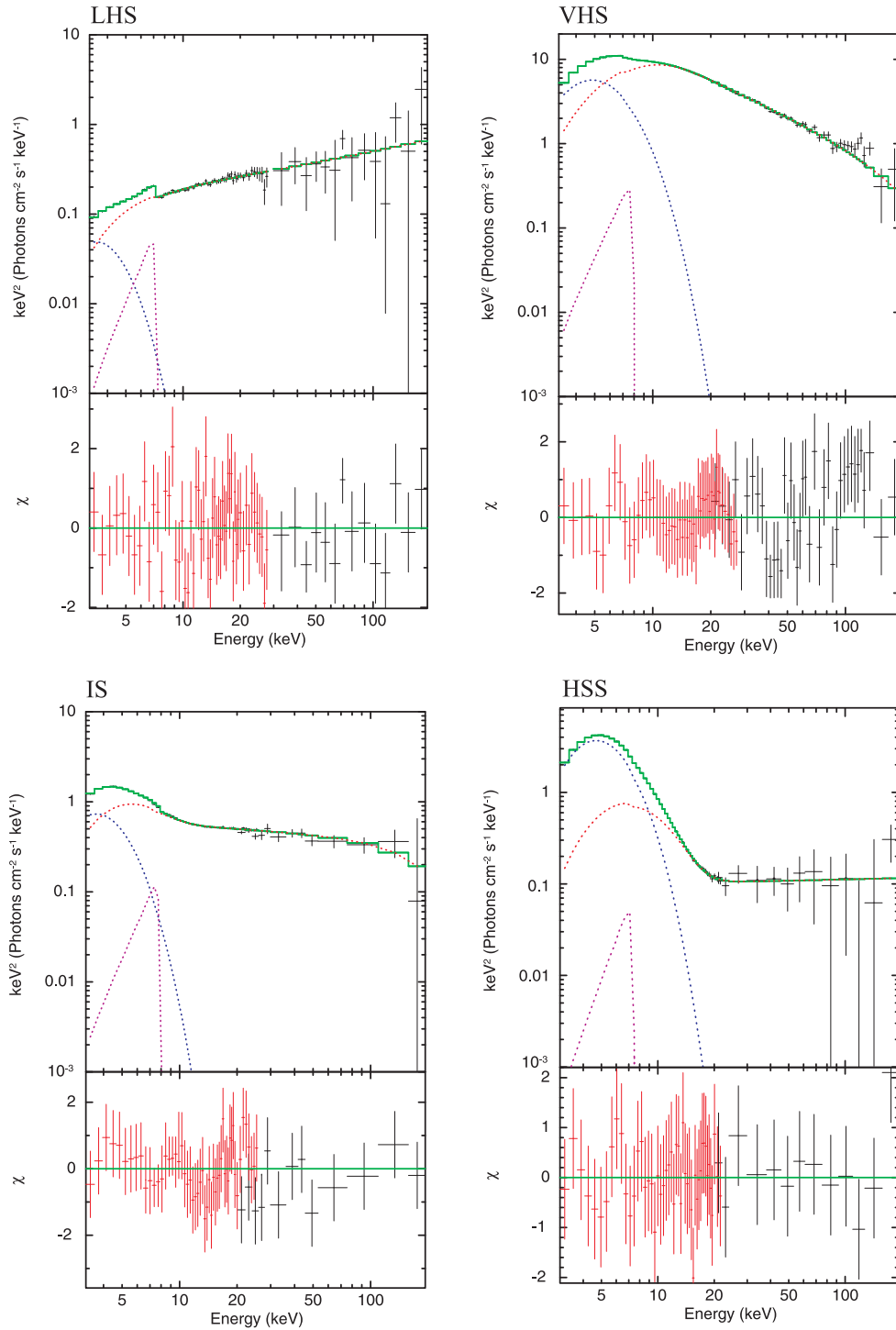
Figure 5. Evolution of spectral diagrams of 4U 1630–47. Data are taken from *RXTE* observations 30172-01-18-12 ($\Gamma = 1.6$, LHS), 30172-01-04-00 ($\Gamma = 2.2$, IS), 80117-01-05-00 ($\Gamma = 3.0$, VHS), and 10411-01-03-00 ($\Gamma = 2.0$, HSS). Here data are denoted by black points; the spectral model presented with components is shown by blue, red, and purple lines for *Blackbody*, *Comptb*, and *Laor* components, respectively.

(A color version of this figure is available in the online journal.)

model is presented by *blackbody*, *Comptb*, and *Laor* components shown by blue, red, and purple lines, respectively.

The best-fit model parameters for the LHS state (top left panel) are $\Gamma = 1.62 \pm 0.03$, $kT_e = 49 \pm 6$ keV, and $E_{\text{line}} = 5.86 \pm 0.06$ keV ($\chi^2_{\text{red}} = 1.00$ for 93 dof); the best-fit model parameters for the IS state (bottom left panel) are $\Gamma = 2.15 \pm 0.02$, $kT_e = 41 \pm 5$ keV, and $E_{\text{line}} = 6.40 \pm 0.02$ keV ($\chi^2_{\text{red}} = 1.35$ for 93 dof); the best-fit model parameters for the VHS state (top right panel) are $\Gamma = 2.98 \pm 0.01$, $kT_e > 200$ keV, and

$E_{\text{line}} = 6.44 \pm 0.07$ keV ($\chi^2_{\text{red}} = 0.97$ for 93 dof); and, finally, the best-fit model parameters for the HSS state (bottom right panel) are $\Gamma = 1.9 \pm 0.8$, $kT_e = 59 \pm 1$ keV, and $E_{\text{line}} = 6.41 \pm 0.05$ keV ($\chi^2_{\text{ref}} = 0.65$ for 93 dof).

Thus, *RXTE* observations cover 4U 1630–47 in four spectral states and reveal its spectral evolution from the low-hard to high-soft states. In Figure 6 we illustrate the spectral evolution for the LHS-IS-VSS-VHS transition using six representative EF_E spectral diagrams that are related to these spectral states in

Table 3
Best-fit Parameters of Spectral Analysis of *BeppoSAX* Observations of 4U 1630–47 in 0.3–200 keV Energy Range[a]

Observational ID	MJD, (day)	$\alpha = \Gamma - 1$	$\log(A)$	N_{Com}[b]	T_s, (keV)	kT_e, (keV)	kT_{BB}, (keV)	N_{BB}[b]	E_{line}, (keV)	N_{line}[b]	N_H, (cm^{-2})	χ^2_{red} (dof)
20114001	50864.238	1.68(2)	0.02(1)	12.86(4)	1.49(4)	>200	0.75(2)	8.24(7)	6.51(4)	0.82(7)	7.5(1)	1.05(127)
20114002	50868.254	1.62(5)	−0.18(3)	11.83(3)	1.48(3)	>200	0.74(2)	8.76(6)	6.42(4)	0.81(8)	7.8(1)	1.16(127)
20114003	50879.516	1.57(6)	−0.15(5)	11.03(4)	1.64(5)	>200	0.74(2)	13.64(5)	5.77(8)	0.65(4)	7.2(3)	1.08(127)
20114004	50891.620	1.00(1)	−0.04(2)	1.80(2)	1.46(6)	50(2)	0.75(3)	3.98(4)	7.19(3)	0.16(2)	6.6(2)	1.10(127)
20114005	50898.720	1.03(3)	0.20(5)	1.44(2)	1.01(7)	58(1)	0.62(5)	1.96(4)	7.08(6)	0.16(7)	6.6(2)	1.18(127)
70566001	51031.516	0.97(5)	2.0[c]	0.59(3)	1.6(1)	140(20)	0.75(5)	0.49(4)	5.26(4)	0.10(1)	6.9(3)	1.15(128)
70821005	51398.857	1.01(2)	0.02(1)	2.20(3)	1.6(2)	160(50)	0.72(9)	0.07(2)	5.38(5)	0.10(2)	6.9(1)	0.92(127)

Notes. Parameter errors correspond to 90% confidence level.
[a] The spectral model is *wabs* ∗ (*blackbody* + *Comptb* + *Laor*).
[b] Normalization parameters of *blackbody* and *Comptb* components are in units of L_{37}/d_{10}^2 erg s^{-1} kpc^{-2}, where L_{37} is the source luminosity in units of 10^{37} erg s^{-1}, d_{10}^2 is the distance to the source in units of 10 kpc, and the *Laor* component is in units of $10^{-2} \times$ total photons cm^{-2} s^{-1} in line.
[c] When parameter $\log(A) \gg 1$, it is fixed to a value 2.0 (see comments in the text).
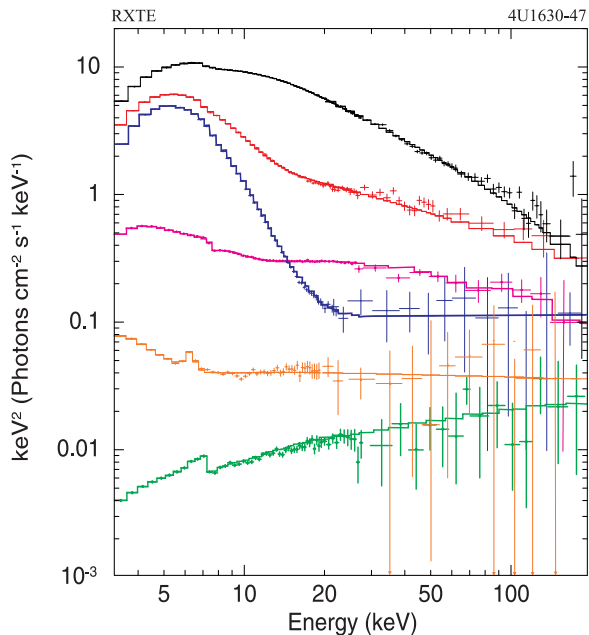

Figure 6. Six representative EF_E spectral diagrams that are related to different spectral states of 4U 1630–47 using the model *wabs* ∗ (*Blackbody* + *Comptb* + *Laor*). The data are taken from *RXTE* observations 30172-01-18-12 (green, LHS), 10411-01-18-00 (orange, LHS), 30172-01-07-00 (pink, IS), 70417-01-03-00 (red, IS), 10411-01-03-00 (blue, HSS), and 80117-01-03-00G (black, VSS). The normalization factors of 0.5 and 0.1 were applied for 10411-01-18-00 and 30172-01-18-12 spectra for clarity.

(A color version of this figure is available in the online journal.)

4U 1630–47. Similarly to our *BeppoSAX* spectral analysis, we use as the best-fit model *wabs* ∗ (*Blackbody* + *Comptb* + *Laor*) for the *RXTE* spectral modeling. The data are taken from *RXTE* observations 30172-01-18-12 (*green*, LHS), 10411-01-18-00 (*orange*, LHS), 30172-01-07-00 (*pink*, IS), 70417-01-03-00 (*red*, IS), 10411-01-03-00 (*blue*, HSS), and 80117-01-03-00G (*black*, VHS). For clarity of the presentation we use the normalization factors of 0.5 and 0.1 for 10411-01-18-00 and 30172-01-18-12 spectra (*orange* and *pink* curves, respectively). An example of the best-fit parameters of the source spectrum and values of χ^2_{red} including the number of degrees of freedom for *RXTE* spectra is presented in Table 4 for 1998 (*R*2 set). In particular, we find that the illumination fraction *f* of the *Comptb* component varies in a wide range between 0 and 1, and that it undergoes sudden changes during an outburst phase for all observations.

In general, for the VHS events (see blue line in Figure 6) are characterized by a dominant soft *blackbody* component and relatively weak power-law component with respect to that in the IS and VSS. In the IS and VSS spectra the contribution of the *blackbody* component is less than that for the VHS. In the LHS spectrum, the Comptonization component is dominant and the *blackbody* component is weak, in agreement with our the *BeppoSAX* analysis. An evolution between the low state and high state is accompanied by a monotonic increase of the normalization parameter N_{com} of the Compton component from 0.1 to $30 \times L_{37}/d_{10}^2$ erg s^{-1} kpc^{-2} and by an increase of the photon index Γ from 1.5 to 3 (see Figure 7). We should point out a clear anti-correlation between the illumination fraction and the photon index, identified by Stiele et al. (2013, combine their Figure 4, middle panels) for XTE J1650–500. Our results show that for 4U 1630–47 the illumination fraction *f* and the index Γ also anti-correlate in a similar manner (compare Figure 7 and Figure 4 in Stiele et al. 2013).

T05 reported a strong bump at ∼20 keV in some *RXTE* spectra of 4U 1630–47, which cannot be satisfactorily fit with their adopted model [*wabs*∗(*diskbb*+*cutoffpl*+*Gaussian*)∗*smedge*]. In our investigation we find small positive excess at 20 keV for only one particular *RXTE* observation (ID = 50135-02-03-00) studied by T05.

Previous analyses of other X-ray binaries occasionally show a clear bump at 20 keV in their IS spectra. We suggest that it is difficult to explain this feature purely in terms of Compton reflection because the photon index $\Gamma > 2$ and thus there is a lack of photons in the incident spectrum to effectively form this 20 keV reflection bump. In fact, this feature can be more naturally attributed to the reprocessing of high-energy photons into lower energies due to down-scattering off relatively cold electrons in the surrounding disk or cold outflow if Γ is less than 2 (see Basko et al. 1974; Laurent & Titarchuk 2007). Laurent & Titarchuk (2007) demonstrate using a Monte Carlo simulation and theoretical arguments that the reflection bump never appears in the emergent spectra if the photon index of the spectrum Γ is higher than 2. The resulting spectrum becomes steeper and the spectrum is deformed.

An additional thermal component with a relatively high color temperature of about 4–5 keV (a so-called *high-temperature blackbody* component; see, e.g., TS09; Seifina & Titarchuk 2010, hereafter ST10; Koljonen et al. 2013; Mineo et al. 2012) is a component of the spectral model that fits the data. TS09 find eight IS and VHS spectra of GRS 1915+105 that require this *high-temperature blackbody* component. These cases are

Table 4
Best-fit Parameters of Spectral Analysis for 1998 ("R2" set) with PCA&HEXTE/RXTE Observations of 4U 1630–47 in 3–200 keV Energy Range[a]

Observational ID	MJD (day)	$\alpha = \Gamma - 1$	kT_e (keV)	$\log(A)$[b]	N_{com}[c]	T_s (keV)	N_{Bbody}[c]	E_{line} (keV)	N_{line}[c]	χ^2_{red} (dof)	F_1/F_2[d]
30178-01-01-00	50853.057	1.06(1)	48(8)	0.92(8)	2.18(6)	1.00(6)	1.06(9)	6.10(9)	0.63(9)	1.41(93)	1.97/3.17
30178-01-02-00	50853.655	1.47(9)	60 ± 10	2.00[b]	4.2(1)	1.9(2)	3.0(1)	5.9(1)	0.19(7)	0.73(94)	2.61/3.82
30178-02-01-00	50855.046	1.23(1)	50 ± 10	2.00[b]	8.08(9)	1.03(9)	1.14(5)	6.40(6)	0.13(6)	1.43(94)	5.14/5.96
30188-02-01-00	50855.428	1.28(2)	43(3)	2.00[b]	8.04(5)	1.13(8)	3.56(9)	6.41(3)	0.16(6)	1.25(94)	5.53/6.22
30178-01-03-00	50855.841	1.54(4)	70 ± 20	1.01(9)	7.5(1)	1.9(1)	7.89(9)	5.61(3)	0.03(8)	0.90(93)	6.19/6.10
30188-02-02-00	50856.115	1.30(2)	52(3)	2.00[b]	8.5(1)	1.13(9)	4.2(1)	6.40(6)	0.18(6)	0.86(94)	5.95/6.24
30188-02-04-00	50856.502	1.36(2)	51(7)	2.00[b]	9.2(1)	1.13(8)	4.6(1)	6.39(2)	0.19(4)	1.32(94)	6.55/6.39
30178-01-04-00	50856.627	1.58(4)	50 ± 10	1.62(9)	7.5(1)	1.9(2)	7.98(9)	5.67(3)	0.06(9)	1.27(93)	6.42/6.16
30188-02-03-00	50856.651	1.37(2)	54(4)	2.00[b]	8.9(1)	1.13(9)	4.6(1)	6.42(6)	0.21(9)	1.18(94)	6.38/6.25
30178-02-01-01	50856.869	1.48(2)	54(3)	2.00[b]	10.0(1)	1.02(9)	3.29(5)	6.41(7)	0.19(6)	1.26(94)	6.54/6.38
30178-01-05-00	50857.116	1.64(6)	90 ± 20	2.00[b]	7.5(1)	1.9(1)	8.64(1)	5.70(2)	0.08(2)	1.24(94)	6.84/6.04
30188-02-05-00	50857.709	1.58(2)	134(7)	0.92(1)	9.16(9)	1.12(9)	4.99(8)	6.42(3)	0.19(6)	0.89(93)	6.57/5.04
30178-02-02-00	50857.793	1.54(3)	105(5)	2.00[b]	10.1(1)	1.03(8)	4.03(8)	6.41(5)	0.14(7)	0.81(94)	6.85/5.35
30188-02-06-00	50858.045	1.46(2)	102(6)	2.00[b]	9.57(9)	1.13(9)	4.69(9)	6.40(6)	0.12(7)	0.73(94)	6.72/5.76
30178-01-06-00	50858.694	1.62(5)	70 ± 20	2.00[b]	7.6(1)	1.9(1)	8.49(1)	5.73(3)	0.11(9)	0.71(94)	6.92/5.78
30188-02-07-00	50858.715	1.49(2)	105(8)	2.00[b]	9.83(9)	1.14(8)	4.86(9)	6.44(8)	0.16(6)	0.80(94)	6.93/5.77
30178-02-02-01	50858.771	1.53(1)	113(6)	2.00[b]	9.97(7)	1.03(9)	4.07(4)	6.40(5)	0.18(5)	1.39(94)	6.79/5.65
30178-01-07-00	50859.836	1.72(5)	50 ± 20	2.00[b]	7.6(1)	1.85(8)	9.19(8)	5.89(6)	0.08(9)	0.73(94)	7.28/5.35
30188-02-08-00	50860.117	1.55(3)	118(3)	0.79(9)	10.7(1)	1.13(9)	4.51(9)	6.40(2)	0.19(6)	0.80(93)	7.16/5.13
30188-02-09-00	50860.562	1.60(4)	148(7)	2.00[b]	9.9(1)	1.12(7)	5.6(1)	6.40(5)	0.19(8)	0.92(94)	7.30/5.69
30178-01-08-00	50860.722	1.70(4)	160 ± 20	2.00[b]	7.7(2)	1.9(1)	9.46(9)	5.50(6)	0.11(7)	0.82(94)	7.40/5.97
30178-01-09-00	50861.693	1.70(4)	130(8)	2.00[b]	9.26(2)	1.67(4)	9.26(2)	6.41(3)	0.19(4)	0.94(94)	7.37/6.02
30188-02-10-00	50861.723	1.52(2)	125(2)	2.00[b]	9.98(9)	1.13(8)	5.5(1)	6.40(2)	0.19(6)	0.93(94)	7.36/5.98
30178-01-10-00	50862.653	1.71(4)	165(5)	2.00[b]	7.85(2)	2.0(2)	9.52(2)	6.41(6)	0.14(6)	0.95(94)	7.50/5.88
30188-02-11-00	50862.704	1.51(2)	125(3)	2.00[b]	10.1(1)	1.12(8)	5.7(1)	6.41(4)	0.11(5)	0.94(94)	7.41/6.04
30178-02-03-00	50862.765	1.54(1)	96(4)	2.00[b]	10.95(9)	1.07(9)	5.05(9)	6.40(5)	0.13(3)	1.09(94)	7.65/6.22
30178-01-11-00	50863.695	1.71(4)	127(7)	0.64(9)	9.50(1)	1.7(2)	12.38(1)	6.43(4)	0.18(5)	0.93(93)	9.40/5.44
30188-02-12-00	50863.712	1.87(3)	180 ± 20	0.66(8)	14.7(1)	1.12(8)	5.5(1)	6.41(4)	0.21(8)	0.90(93)	9.46/5.51
30188-02-13-00	50864.185	1.87(4)	125(4)	0.91(9)	15.97(1)	1.13(9)	5.8(1)	6.47(3)	0.19(5)	0.87(93)	10.30/7.24
30188-02-14-00	50864.320	1.92(3)	>200	1.3(1)	12.9(1)	1.14(7)	5.91(8)	6.45(5)	0.15(6)	1.06(93)	8.46/6.00
30178-01-12-00	50864.630	1.70(2)	130(4)	0.28(3)	9.22(6)	1.93(8)	13.99(9)	6.46(2)	0.17(8)	1.09(93)	9.54/5.43
30188-02-15-00	50865.046	1.73(4)	125(7)	0.9(1)	15.98(7)	1.13(9)	5.7(1)	6.40(6)	0.19(6)	0.72(93)	10.24/6.82
30188-02-16-00	50865.320	1.69(3)	161(9)	1.7(1)	11.48(9)	1.12(6)	6.1(1)	6.44(4)	0.13(3)	0.94(93)	8.32/5.90
30188-02-17-00	50866.639	1.70(4)	172(3)	0.25(4)	18.0(1)	1.12(7)	6.0(1)	6.48(5)	0.19(6)	1.21(93)	9.70/5.76
30178-01-13-00	50867.497	1.72(3)	200 ± 40	0.27(7)	8.34(9)	1.92(9)	14.36(9)	6.41(4)	0.14(9)	0.86(93)	9.64/5.44
30188-02-18-00	50868.568	1.88(2)	>200	0.28(4)	15.6(1)	1.14(2)	3.0(1)	6.40(2)	0.19(6)	1.15(93)	9.11/4.66
30188-02-19-00	50869.650	1.78(4)	200 ± 20	0.05(2)	17.7(1)	1.12(7)	6.04(9)	6.42(3)	0.17(1)	1.23(93)	9.13/4.79
30188-02-20-00	50870.181	1.44(1)	70 ± 20	2.00[b]	5.7(1)	1.13(5)	7.7(1)	6.40(4)	0.19(6)	1.13(94)	5.43/3.97
30178-01-14-00	50870.978	1.70(2)	150 ± 30	2.00[b]	4.93(9)	1.98(3)	11.57(9)	6.41(5)	0.18(7)	0.76(94)	6.15/3.77
30188-02-21-00	50871.257	1.53(1)	100 ± 30	2.00[b]	5.9(1)	1.13(9)	8.5(1)	6.43(4)	0.19(6)	0.93(94)	6.22/3.64
30188-02-21-01	50871.410	1.49(2)	100 ± 10	2.00[b]	5.97(9)	1.11(7)	7.9(1)	6.40(4)	0.12(5)	0.91(94)	6.13/3.96
30188-02-22-00	50872.841	1.51(3)	103(7)	2.00[b]	4.87(4)	1.99(7)	8.9(1)	9.47(1)	0.19(6)	0.94(94)	5.84/4.10
30188-02-23-00	50873.138	1.52(2)	126(5)	2.00[b]	4.61(4)	1.47(9)	10.0(1)	8.46(7)	0.11(5)	0.74(94)	6.15/3.35
30178-01-15-00	50874.516	1.54(8)	100 ± 20	0.3(1)	8.92(1)	1.40(4)	7.77(9)	6.40(4)	0.08(6)	1.19(93)	6.97/4.19
30172-01-01-01	50876.184	1.34(4)	56(5)	0.49(9)	7.0(1)	0.99(6)	4.1(2)	6.41(1)	0.06(2)	0.63(94)	5.22/3.68
30172-01-01-02	50877.186	1.29(2)	43(2)	0.10(2)	9.59(3)	1.05(4)	6.74(9)	6.43(2)	0.03(1)	0.82(94)	5.13/3.98
30172-01-01-03	50880.378	1.61(3)	120 ± 20	0.27(7)	12.6(2)	1.11(6)	5.51(8)	6.40(1)	0.04(8)	0.66(94)	6.58/4.72
30172-01-01-04	50881.378	1.69(2)	50 ± 10	0.33(8)	14.1(2)	1.05(8)	1.8(1)	6.49(4)	0.03(4)	1.12(93)	7.33/4.78
30178-01-16-00	50881.580	1.54(8)	130 ± 10	0.3(1)	8.92(1)	1.4(1)	7.77(9)	6.40(6)	0.19(6)	1.11(93)	6.96/4.19
30172-01-01-00	50883.847	1.51(7)	60 ± 30	0.01(1)	4.8(1)	1.01(6)	5.0(1)	6.44(1)	0.02(1)	1.01(94)	4.24/1.70
30178-01-17-00	50884.981	1.45(3)	100 ± 20	−0.29(8)	7.89(5)	1.00(3)	3.81(9)	6.40(9)	0.19(6)	0.95(93)	3.88/1.76
30172-01-02-01	50885.146	1.20(1)	60(8)	−0.18(2)	6.14(4)	1.10(8)	9.84(5)	6.41(1)	0.04(1)	0.86(93)	3.55/2.14
30172-01-02-00	50885.805	1.27(2)	55(3)	−0.10(2)	5.79(7)	1.10(7)	10.0(1)	6.40(3)	0.02(4)	0.98(93)	3.44/2.06
30172-01-03-00	50887.714	1.22(1)	43(4)	−0.07(3)	4.6(1)	1.07(5)	4.41(9)	6.43(2)	0.03(2)	1.04(93)	3.08/1.75
30178-01-18-00	50889.714	1.30(3)	55(4)	−0.23(5)	4.74(6)	1.00(3)	3.48(7)	6.44(6)	0.19(6)	1.07(93)	2.90/1.34
30172-01-05-00	50891.646	1.13(1)	43(2)	−0.07(4)	3.21(8)	1.07(5)	4.02(8)	6.41(1)	0.03(1)	1.35(93)	2.27/1.35
30172-01-04-00	50892.584	1.15(2)	41(5)	−0.11(4)	3.15(8)	1.07(6)	4.01(8)	6.40(2)	0.04(3)	1.35(93)	2.22/1.28
30172-01-06-00	50893.719	1.17(3)	50(7)	−0.36(9)	4.04(5)	0.99(4)	2.91(7)	6.45(6)	0.02(1)	0.89(93)	2.09/1.09
30172-01-07-00	50895.651	1.11(2)	45(2)	0.39(6)	1.86(8)	1.23(9)	2.67(9)	6.50(1)	0.07(2)	1.14(93)	1.62/1.35
30178-01-19-00	50897.802	1.15(2)	48(6)	0.36(4)	2.44(5)	1.00(3)	2.70(8)	6.42(3)	0.19(6)	1.05(93)	1.40/1.15
30172-01-08-00	50899.001	0.96(5)	56(6)	0.03(2)	1.82(9)	1.30(9)	3.38(9)	6.50(1)	0.06(1)	1.22(93)	1.36/1.10
30172-01-08-02	50900.675	1.01(3)	50(7)	0.18(6)	1.6(1)	1.31(8)	2.9(1)	5.74(2)	0.07(2)	0.85(93)	1.15/1.04
30410-02-06-00	50900.747	1.00(4)	90 ± 20	2.00[b]	3.14(1)	1.27(9)	3.0(1)	5.9(1)	0.01(9)	1.17(94)	0.18/0.34
30178-01-20-00	50903.139	1.08(3)	51(5)	−0.01(1)	1.90(5)	1.00(3)	2.38(9)	6.40(5)	0.19(6)	1.29(93)	1.08/0.93
30172-01-08-03	50904.209	1.17(4)	50(8)	−0.12(4)	1.87(2)	1.01(8)	3.1(1)	6.34(6)	0.07(5)	1.01(93)	1.02/0.85

9

Table 4
(Continued)

Observational ID	MJD (day)	$\alpha = \Gamma - 1$	kT_e (keV)	$\log(A)$[b]	N_{com}[c]	T_s (keV)	N_{Bbody}[c]	E_{line} (keV)	N_{line}[c]	χ^2_{red} (dof)	F_1/F_2[d]
30172-01-09-00	50904.525	0.91(3)	51(1)	0.08(2)	1.5(1)	1.29(5)	3.58(2)	6.36(7)	0.04(6)	1.05(93)	1.00/0.96
30172-01-10-00	50906.513	0.99(1)	50(3)	0.2(1)	1.6(1)	1.20(4)	3.67(9)	6.56(6)	0.08(3)	1.39(93)	0.92/1.08
30172-01-11-00	50907.511	1.00(1)	49(5)	0.17(8)	1.57(9)	1.24(3)	3.76(8)	6.57(3)	0.11(6)	1.20(93)	0.89/1.04
30172-01-12-00	50909.410	1.00(2)	50(3)	0.11(4)	1.59(7)	1.00(5)	3.88(2)	5.9(2)	0.07(5)	0.91(93)	0.89/0.98
30172-01-13-00	50911.309	1.06(3)	44(4)	−0.07(8)	1.6(1)	1.09(3)	3.91(9)	6.5(1)	0.09(6)	0.73(93)	0.91/0.73
30172-01-14-00	50913.311	1.00(1)	51(2)	−0.22(5)	1.54(9)	1.11(2)	3.6(1)	5.98(9)	0.03(7)	0.69(93)	0.88/0.61
30172-01-08-04	50921.580	0.93(7)	50(6)	0.10(8)	1.74(5)	1.01(9)	3.49(9)	6.34(6)	0.05(6)	1.14(93)	0.96/1.15
30172-01-15-00	50923.598	1.05(2)	55(3)	−0.13(4)	1.91(9)	1.08(2)	3.61(6)	7.6(2)	0.01(3)	0.73(93)	0.96/0.82
30172-01-16-00	50924.744	1.03(2)	47(2)	−0.09(4)	2.1(1)	1.09(3)	3.24(6)	6.8(1)	0.06(8)	1.00(93)	1.01/0.97
30172-01-17-00	50925.857	1.03(4)	50 ± 10	0.13(7)	1.7(1)	1.06(8)	2.38(9)	6.82(8)	0.02(6)	1.03(93)	1.05/1.03
30172-01-17-01	50926.653	0.89(3)	60 ± 10	0.06(3)	1.9(1)	1.07(7)	2.4(1)	6.79(3)	0.01(5)	1.00(93)	1.10/1.19
30172-01-17-02	50927.722	1.1(1)	72 ± 20	0.03(3)	1.82(9)	1.05(9)	2.6(1)	6.80(4)	0.06(3)	0.99(93)	1.17/0.95
30172-01-17-03	50928.591	1.22(6)	90 ± 20	0.05(4)	1.98(9)	1.01(7)	2.48(9)	6.83(8)	0.04(6)	1.10(93)	1.19/0.90
30172-01-17-04	50929.657	1.10(6)	100 ± 20	−0.04(2)	2.0(1)	1.07(6)	2.64(7)	6.84(5)	0.05(5)	0.90(93)	1.22/0.93
30172-01-17-05	50930.657	1.07(6)	90 ± 20	−0.13(7)	2.2(1)	1.05(7)	2.82(9)	6.80(8)	0.03(6)	0.89(93)	1.28/0.92
30172-01-17-06	50931.859	1.09(7)	50 ± 10	0.09(7)	1.7(1)	1.05(7)	2.05(8)	6.81(8)	0.07(8)	1.03(93)	1.13/0.94
30172-01-17-07	50932.793	1.10(5)	90 ± 10	−0.02(9)	2.34(9)	1.02(8)	2.64(9)	6.82(3)	0.08(7)	1.05(93)	1.35/1.11
30172-01-18-00	50935.127	1.08(3)	110 ± 20	−0.16(8)	2.6(1)	0.99(5)	2.69(7)	6.80(2)	0.11(6)	0.78(93)	1.42/1.04
30172-01-18-01	50936.194	1.15(5)	90 ± 10	−0.25(9)	2.6(1)	0.97(6)	2.65(6)	6.80(8)	0.09(9)	0.84(93)	1.39/0.85
30172-01-18-02	50937.622	1.06(7)	80 ± 10	−0.14(8)	2.25(8)	1.08(7)	3.16(9)	6.82(6)	0.04(6)	0.88(93)	1.41/0.96
30172-01-18-03	50939.061	1.00(4)	90 ± 10	−0.05(9)	2.0(1)	1.14(6)	3.05(9)	6.85(8)	0.07(2)	0.84(93)	1.32/1.01
30172-01-18-04	50942.015	0.81(7)	50 ± 20	−0.08(7)	1.38(9)	1.2(1)	2.6(1)	6.86(7)	0.03(6)	1.05(93)	1.09/0.81
30172-01-18-05	50945.860	0.9(1)	90 ± 10	0.14(9)	1.2(1)	1.3(1)	5.98(8)	6.60(9)	0.02(5)	1.33(93)	0.93/0.76
30172-01-18-06	50945.861	1.01(5)	40 ± 10	0.2(1)	0.99(2)	1.21(6)	2.46(9)	6.84(8)	0.03(6)	1.32(93)	0.71/0.67
30172-01-18-07	50949.732	0.89(7)	50 ± 10	0.24(7)	0.92(2)	1.39(5)	2.24(6)	5.99(9)	0.06(6)	1.01(93)	0.64/0.69
30172-01-18-08	50951.661	0.93(2)	60 ± 10	2.00[b]	0.91(4)	1.00(6)	0.91(6)	6.21(7)	0.03(4)	0.87(94)	0.59/1.05
30172-01-18-09	50952.482	0.86(3)	40 ± 10	2.00[b]	0.83(3)	1.00(7)	0.78(5)	6.18(7)	0.33(6)	1.46(94)	0.52/1.03
30172-01-18-10	50953.983	0.77(2)	50 ± 10	2.00[b]	0.62(2)	1.00(3)	0.62(4)	6.03(6)	0.21(5)	1.12(94)	0.42/0.91
30172-01-18-11	50956.949	0.87(4)	50 ± 10	2.00[b]	0.45(3)	1.00(6)	0.35(5)	6.1(1)	0.20(6)	1.43(94)	0.28/0.55
30172-01-18-12	50958.950	0.62(3)	49(6)	2.00[b]	0.47(4)	1.00(7)	0.41(5)	5.86(6)	0.27(9)	1.00(94)	0.28/0.72
30172-01-18-13	50961.087	0.71(6)	50(8)	2.00[b]	0.45(5)	1.00(1)	0.33(9)	6.2(1)	0.18(2)	0.82(94)	0.27/0.65
30172-01-18-14	50962.949	0.64(3)	46(6)	2.00[b]	0.59(3)	1.00(8)	0.24(6)	5.9(1)	0.18(6)	1.42(94)	0.32/0.89
30172-01-18-15	50965.948	0.23(3)	148(9)	2.00[b]	0.31(4)	1.00(6)	0.31(5)	5.84(9)	0.11(5)	0.83(94)	0.28/0.69
30172-01-18-16	50968.261	0.49(3)	50(3)	2.00[b]	0.47(3)	1.00(7)	0.30(5)	5.84(9)	0.18(7)	1.21(94)	0.27/0.68
30172-01-18-17	50970.387	0.52(4)	50(5)	2.00[b]	0.42(4)	1.00(4)	0.28(6)	5.9(1)	0.17(5)	1.17(94)	0.24/0.65
30172-01-18-18	50972.126	0.59(2)	54(7)	2.00[b]	0.52(2)	1.00(6)	0.19(5)	6.04(8)	0.18(4)	1.39(94)	0.28/0.82
30410-02-05-00	50988.772	1.19(5)	79(2)	2.00[b]	4.61(4)	1.47(9)	10.0(1)	8.46(9)	0.01(9)	0.18(94)	0.18/0.34
30410-02-07-00	50990.885	0.35(3)	85(8)	2.00[b]	0.26(9)	0.82(9)	0.18(9)	7.14(8)	0.19(6)	0.86(94)	0.18/0.41

Notes. Parameter errors correspond to 90% confidence level.

[a] The spectral model is *wabs* ∗ (*blackbody* + *Comptb* + *Laor*), where N_H is fixed at a value 7.7×10^{22} cm^{-2} (Dieters et al. 2000); kT_{BB} are fixed at 0.7 keV (see comments in the text).

[b] When parameter $\log(A) \gg 2$, this parameter is fixed at 2.0 (see comments in the text).

[c] Normalization parameters of *blackbody* and *Comptb* components are in units of $10^{-2} \times L_{37}/d_{10}^2$ erg s^{-1} kpc^{-2}, where L_{37} is the source luminosity in units of 10^{37} erg s^{-1}, d_{10}^2 is the distance to the source in units of 10 kpc, and the *Laor* component is in units of $10^{-2} \times$ total photons cm^{-2} s^{-1} in line.

[d] Spectral fluxes (F_1/F_2) in units of $\times 10^{-9}$ erg s^{-1} cm^{-2} for (3–10) and (10–50) keV energy ranges, respectively.

rather related to epochs of radio-loud events. Recently, Mineo et al. (2012) find that spectra in the "heartbeat" state of GRS 1915+105 can be fit with models including a *high-temperature blackbody* component of the color temperature 3–6 keV. Furthermore, ST10 reveal 24 IS spectra from SS 433 during radio outburst decay events that had also a strong *high-temperature blackbody* component with color temperature of 4–5 keV. One can suggest that this high-temperature thermal component is indicative of the NS. However, it is well known that an NS color temperature is in the range 1–2.5 keV (see, e.g., Lewin et al. 1997). TS09 argue that this *high-temperature blackbody* bump could be a result of the gravitationally redshifted annihilation line that is initially formed in the close vicinity of a BH horizon.

We should note that a low excess at 10–20 keV in the spectrum residuals for 4U 1630–47 can be excluded (in terms of the χ^2 criterion) if we increase kT_s and kT_{BB} temperatures from

0.6 keV and 1.2 keV correspondingly to 0.7 keV and 1.4 keV, changing the normalization parameters. Thus, we do not find any significant difference in χ^2 with or without a *high-temperature blackbody component*. Both models show acceptable values of $\chi^2_{red} \sim 1$. As a result, we decide to apply an additive model *wabs* ∗ (*Bbody* + *Comptb* + *Laor*) that uses fewer spectral components.

3.3. Discussion of the Data Analysis and X-ray Spectral Modeling

Our spectral model applied to the data from *BeppoSAX* and *RXTE* shows robust performance throughout all data sets. Namely, the value of the reduced χ^2_{red} is less than or around 1.0 for most observations. For a small fraction (less than 3%) of the analyzed spectra with high counting statistics χ^2_{red} reaches 1.5. Note that the energy range for the cases in which we obtain
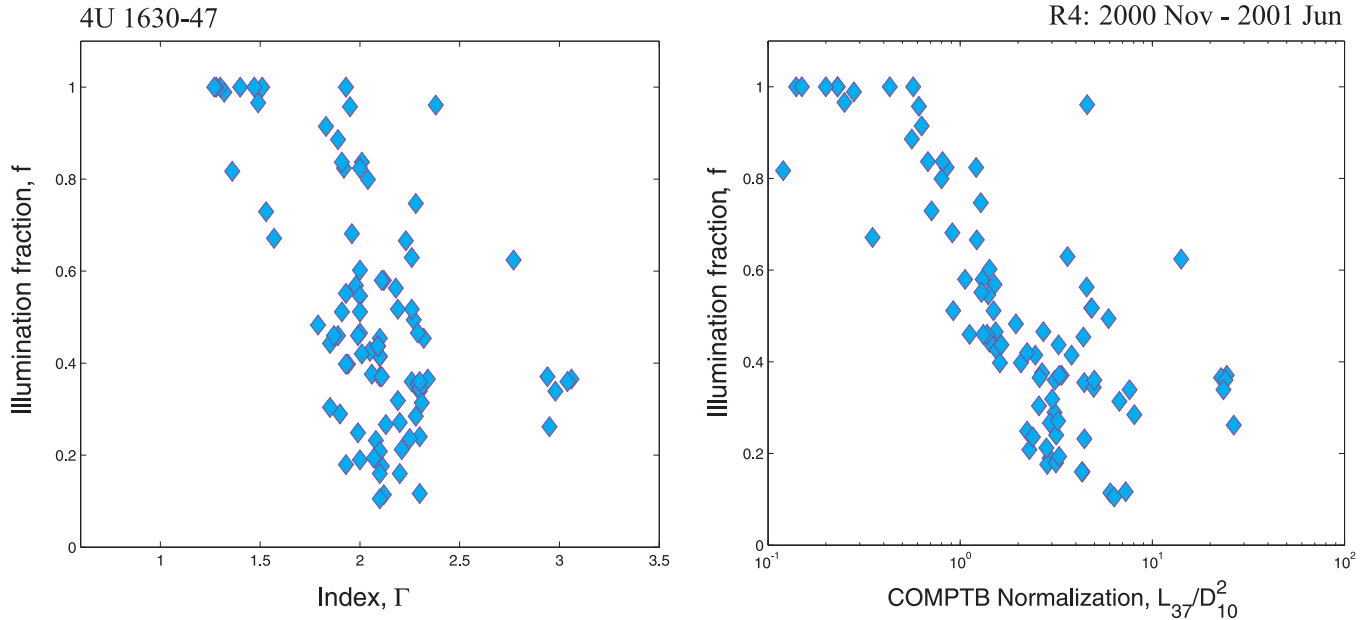
Figure 7. Example of the illumination fraction f vs. the photon index Γ (left) and COMPTB normalization (right) for an observational set $R4$ (2000 November–2001 June).

(A color version of this figure is available in the online journal.)

the poor fit statistic (two among 425 spectra with $\chi^2 = 1.55$ for 93 dof) is related to the iron-line region.

We remind the reader that the iron emission feature at 6–8 keV is clearly detected in *low* (luminosity) states and barely seen in *high* (luminosity) states of 4U 1630–47. Some previous studies (Oosterbroek et al. 1998; Trudolyubov et al. 2001) did not utilize any iron emission line component. Furthermore, Tomsick et al. (1998) pointed out absorption lines from highly ionized H-like and He-like iron lines, which possibly indicate the presence of a highly ionized disk or a wind (see also Kubota et al. 2007). Generally, for sources at a higher inclination, the obscuration of the continuum from the central source by the disk rim allows the detection of wind or the photoionized atmosphere due to observations of narrow emission lines, which are not visible at lower inclinations due to the stronger continuum emission. Recently, Dìaz Trigo et al. (2013) detected highly ionized absorption lines from Fe XXV and Fe XXVI in *XMM-Newton* observations of 4U 1630–47. They discussed a possible origin of these lines in terms of the accretion disk wind. In turn, Ponti et al. (2012) suggested that such winds can significantly affect the resulting X-ray emission of BHs, particularly for high-inclined BHC binary systems. In addition, Cui et al. (2000) detected a double structure of the emission feature fit by two *Gaussian* lines centered around 5.7 and 7.7 keV using the additive continuum model consisting of *multicolor disk* ("diskbb") and *power-law* utilizing *RXTE* data. However, we do not find any evidence of double line structure in the X-ray spectrum of 4U 1630–47 in the framework of our model [$wabs * (Bbody + Comptb + Laor)$].

It is important to point out that we find similar best-fit model parameters with those presented in the literature for the same *BeppoSAX* observations. In particular, the photon index Γ, estimated by Oosterbroek et al. (1998) for observations $S1 - S4$, is about 2–2.7 (both for two additive models: a *power − law + diskblackbody* model and a *pexriv + diskblackbody* model). This similarity of the index values to our results using these different models is indicative of a correct

approach for X-ray spectrum modeling and the spectral state evolution scenario.

Thus, our *Bbody + Comptb + Laor* model shows good performance when we apply it to the observed spectra from 4U 1630–47. In particular, LT99 argue that Generic Comptonization spectra (GCSs) can be formed as a result of the combined *thermal* and *bulk* Comptonization effects. The difference between *Comptb* and GCSs is in the way they explain the exponential cutoff of the spectrum, which is determined by electron energy kT_e in the *Comptb* case and by the plasma energy (thermal plus bulk) in the GCS case. Thus, the *Comptb* model is applicable to the GCS profile with the warning that the meaning of kT_e as the electron temperature can be generalized to include possible effects of bulk-inflow (dynamical) Comptonization. In other words, the cutoff energy can be dictated by the combined effect of thermal and dynamical Comptonization, and the best-fit value of kT_e, in the framework of the *Comptb* component, indeed gives the mean value of the thermal and bulk energy. On the other hand, the energy spectral index α (or the photon index $\Gamma = \alpha + 1$) is a measure of Comptonization efficiency. Indeed, TS09 show that the index α is an inverse of the Comptonization parameter Y, which is a product of average energy change per scattering, $\eta = \langle \Delta E \rangle / E$, and the number of scattering N_{sc} in the medium (Compton region).

We identify, using the *BeppoSAX* observations of 4U 1630–47, the model of the spectrum that covers the broad energy band from 0.3 to 200 keV. On the other hand, the *RXTE* extensive observations give us an opportunity to investigate the overall evolution pattern of the source behavior during all spectral transitions in the 3–200 keV energy range.

4. OVERALL PATTERN OF X-RAY PROPERTIES

Observations of 4U 1630–47 show a variety of different states, which are associated with the changes of X-ray energy and power spectra. Previous investigations of 4U 1630–47 (e.g., Tomsick et al. 2005; Dieters & van der Klis 2000)
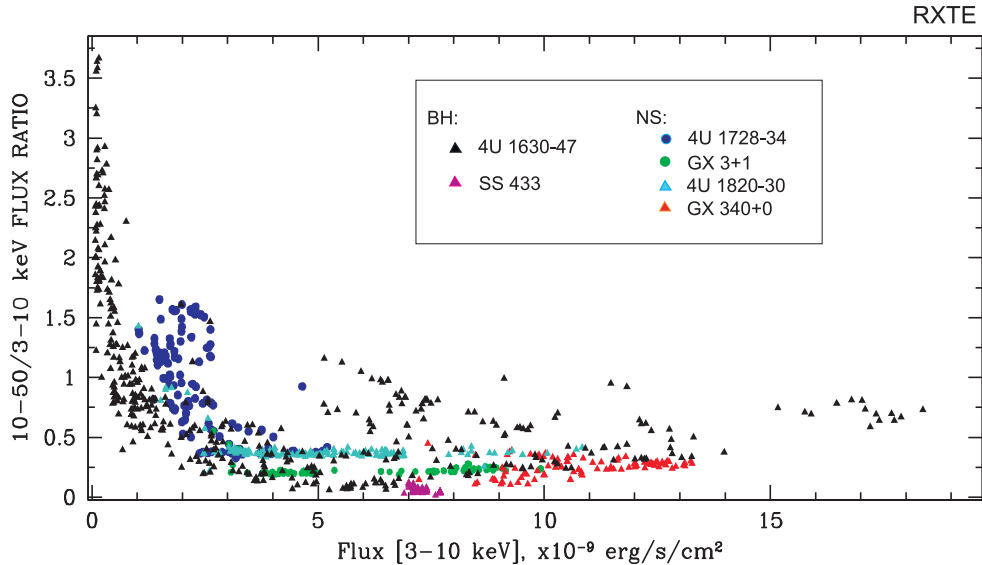
Figure 8. Spectral hardness (10–50 keV/3–10 keV) vs. flux in 3–10 keV range of BHCs: 4U 1630–47 (black triangles), SS 433 (violet triangles, taken from ST10), and NSs: *atoll* sources 4U 1728–34 (blue circles, taken from Seifina & Titarchuk 2011), GX 3+1 (green circles, taken from ST12), and 4U 1820–30 (bright blue triangles), and *Z* source GX 340+0 (red triangles) for *RXTE* data.
(A color version of this figure is available in the online journal.)

highlighted various outburst behavior and also pointed out differences in spectral and timing properties as well as light-curve patterns during individual outbursts. However, Tomsik et al. and Dieters et al. analyzed individual outbursts applying different spectral models, which can introduce corresponding differences in the inferred spectral properties of 4U 1630–47. Therefore, because we are interested in the general character of the spectral evolution of 4U 1630–47, we perform a uniform analysis applying the same spectral model to all observations of 4U 1630–47. As a first step, we construct a hardness–intensity diagram of 4U 1630–47, which helps us to understand how 4U 1630–47 evolves between different spectral states. Note that *the hardness (observable flux ratio) is a measurable quantity and directly related to the index of the spectrum* (see below).

To study the properties of 4U 1630–47 during the spectral transitions, associated with significant changes in source luminosity, we investigate the direct observational dependence of hard color [10–50 keV/3–50 keV] (HC) on the 3–10 keV flux measured in units of 10^{-9} erg s^{-1} cm^{-2} (hardness–intensity diagram (HID)). In Figure 8 we present the flux ratio HC versus the 3–10 keV flux measured in units of 10^{-9} erg s^{-1} cm^{-2} based on the *RXTE* data (*black triangle* points for 4U 1630–47 there). As we see from this figure, the hardness of the spectra monotonically decreases when this energy flux in the 3–10 keV band increases. In other words, the spectrum becomes essentially softer for higher fluxes. The hardness ratio saturates at high flux values, an observational fact that is indicative of the spectral evolution of the source from the LHS through the IS toward the HSS.

As the source moves from the LHS toward the IS, the hard color (HC) drastically drops from 3.7 to 0.1, while the 3–10 keV flux only slightly increases. When the source further moves from the IS toward the soft states (VHS and HSS), the HC saturates while the 3–10 keV flux increases by a factor of 10, i.e., from 2 to 20 × 10^{-9} erg s^{-1} cm^{-2}. In Figure 8 we compare this HC behavior versus the flux for 4U 1630–47 with that observed in other BHCs and NSs.

We use the HC [10–50 keV/3–10 keV] versus flux in the 3–10 keV range in the form of HID for six sources: 4U 1630–473

(BHC, *black*), SS 433 (BHC, *crimson*), 4U 1820–30 (*atoll* NS, *bright blue*), GX 3+1 (*atoll* NS, *green*), 4U 1728–34 (*atoll* NS, *blue*), and GX 340+0 (*Z* type NS, *red*). As one can see from this figure, HID for 4U 1630–47 exhibits two separate branches related to the *hard* spectral states (vertical branch) and to the *soft* states (horizontal branch), whereas all NS sources (except 4U 1728–34) show only the *soft* horizontal branch elongated close to the soft branch of 4U 1630–47. A unique stability (or quasi-constancy) of the hardness ratio for NSs versus the 3–10 keV flux is an observational demonstration for the stability of the photon index Γ established for a number of NS sources (see Farinelli & Titarchuk 2011; Seifina & Titarchuk 2011, 2012; Seifina et al. 2013). This hardness ratio versus the 3–10 keV flux provides a unique diagnostics for the nature of a given compact object.

As evident from this figure, 4U 1630–47 shows both a wider luminosity range and a wider hardness ratio range than any NS source. This observational feature can be related to different rates of mass transfer in NS and BH systems. Thus, the comparison of HIDs, in principle, allows one to probe physical properties of compact objects, in particular, their possible nature, directly related to a shape and localization of HID tracks.

5. EVOLUTION OF X-RAY SPECTRAL PROPERTIES DURING SPECTRAL STATE TRANSITION

A number of X-ray spectral transitions of 4U 1630–47 have been detected by *RXTE* during 1996–2004 (R1–R7 sets). We have searched for common spectral and timing features that can be revealed during these spectral transition events.

The X-ray light curve of 4U 1630–47 shows complex behavior in a wide range of timescales: from seconds to years (e.g., Belloni et al. 1999; T05). Here we discuss the source variability on the timescales of hours. In Figure 9 we demonstrate the source and model parameter evolution for all analyzed outburst spectral transitions. As one can see from the flux panel (second from the top), all outbursts of 4U 1630–47 are characterized by a significant increase of the 3–10 keV flux. Some events also demonstrate an increase of flux in the 10–50 keV energy band (see particular events at MJD 50,860 and 52,260–52,290).
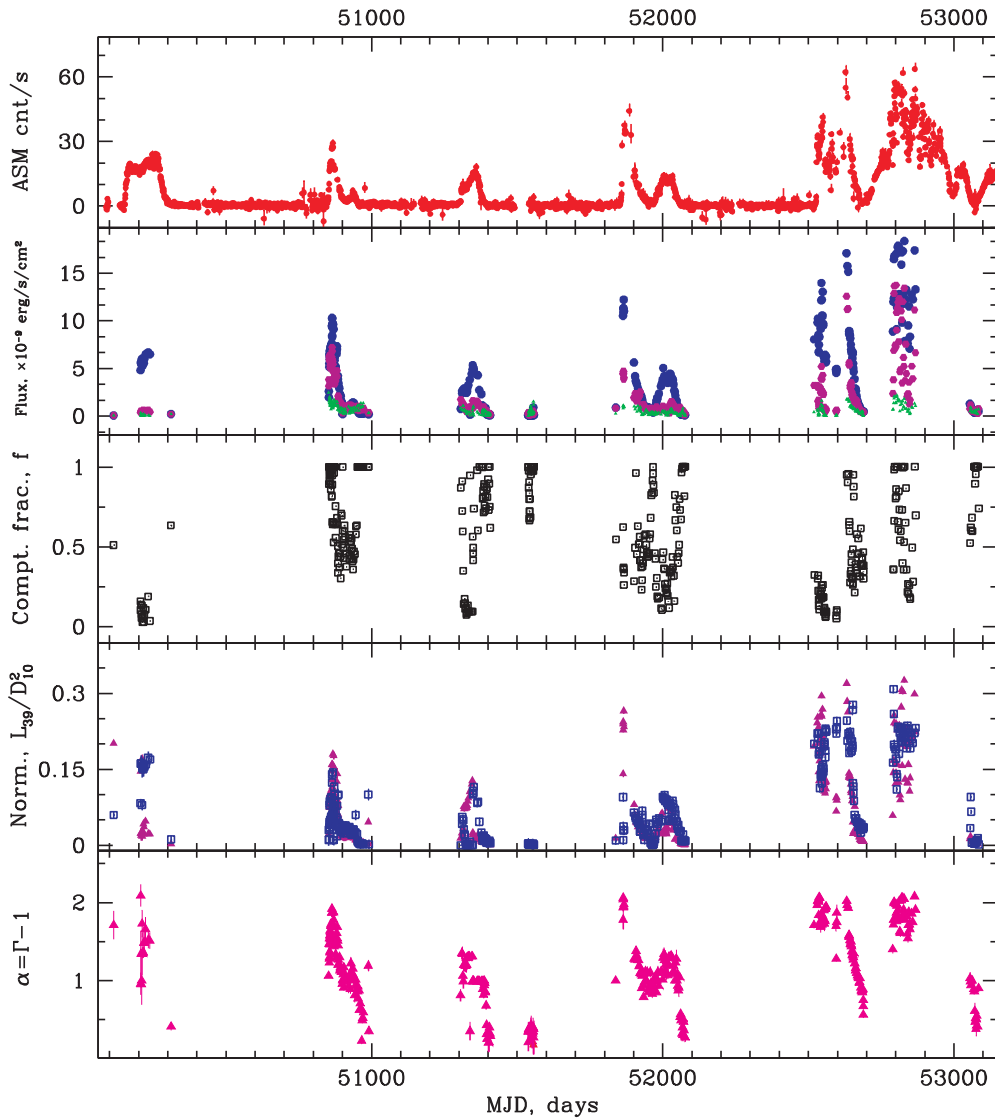
Figure 9. From top to bottom: Evolutions of the *RXTE*/ASM count rate, the model flux in 3–10 keV, 10–50 keV, and 50–200 keV energy ranges (blue, crimson, and green points, respectively), the illumination fraction *f*, and *Comptb* and *blackbody* normalizations (crimson and blue, respectively) for all the *RXTE* sets (*R*1–*R*7, 1996–2004).

(A color version of this figure is available in the online journal.)

For such outbursts with a good rise-decay coverage, the predominance of the 10–50 keV flux over the 3–10 keV flux can be related to a moderate mass accretion rate regime. In fact, the spectral index α is less in these dates (at MJD 50,860 and 52,260–52,290) than that for 2002–2004 (MJD 52,520–53,080) events (see Figure 9). The *pivoting effect* in the 3–10 keV/ 10–50 keV flux relation corresponds to the spectral state change. Namely, in the framework of our spectral model (see Section 3) these spectral transitions are clearly seen as a decrease of the normalization N_{Com} and a spectral index decrease (see Figure 9, two bottom panels at MJD 50,860 and 52,260).

The spectral index $\alpha (= \Gamma - 1)$ is well traced by soft X-ray flux (compare the bottom and two upper panels of Figure 9). Moreover, we do not find any difference in the correlations between Γ and soft X-ray flux for different outbursts, which was previously pointed out by a number of authors (e.g., T05; Trudolyubov et al. 1998). We can also suggest that the 4U 1630–47 spectral state evolution can be traced by the illumination fraction *f*. For example, an excess of the 10–50 keV flux over that for the 3–10 keV energy band (at the low/hard

and intermediate states) mostly occurs for high values of *f* ($0.5 < f < 1$).

The actual difference between outbursts is related to the peak flux reached during an outburst that probably depends on the value of $\dot{M}$. The outbursts can be mainly distinguished by saturation levels achieved at the maximum of individual outbursts (see low panels of Figure 10). Higher saturation levels of the index Γ correspond to higher mass accretion rates. However, the observed index saturation level of Γ never exceeds 3 as predicted by the theoretical calculations of Titarchuk & Zannias (1998). All superimposed index–normalization correlations can be seen in a joint diagram in Figure 11, which provides a generic picture of spectral (index) evolution versus $\dot{M}$ through all outburst activity of 4U 1630–47. We should notice that all outbursts of 4U 1630–47 are associated with *low* radio activity except the 1998 outburst, which is accompanied by strong radio emission (see a possible explanation of the radio activity by Fender 2006 and Corbel et al. 2013). We can suggest that during the 1998 outburst the total mass accretion rate from the companion was so high that some part of this mass flux went to the outflow,
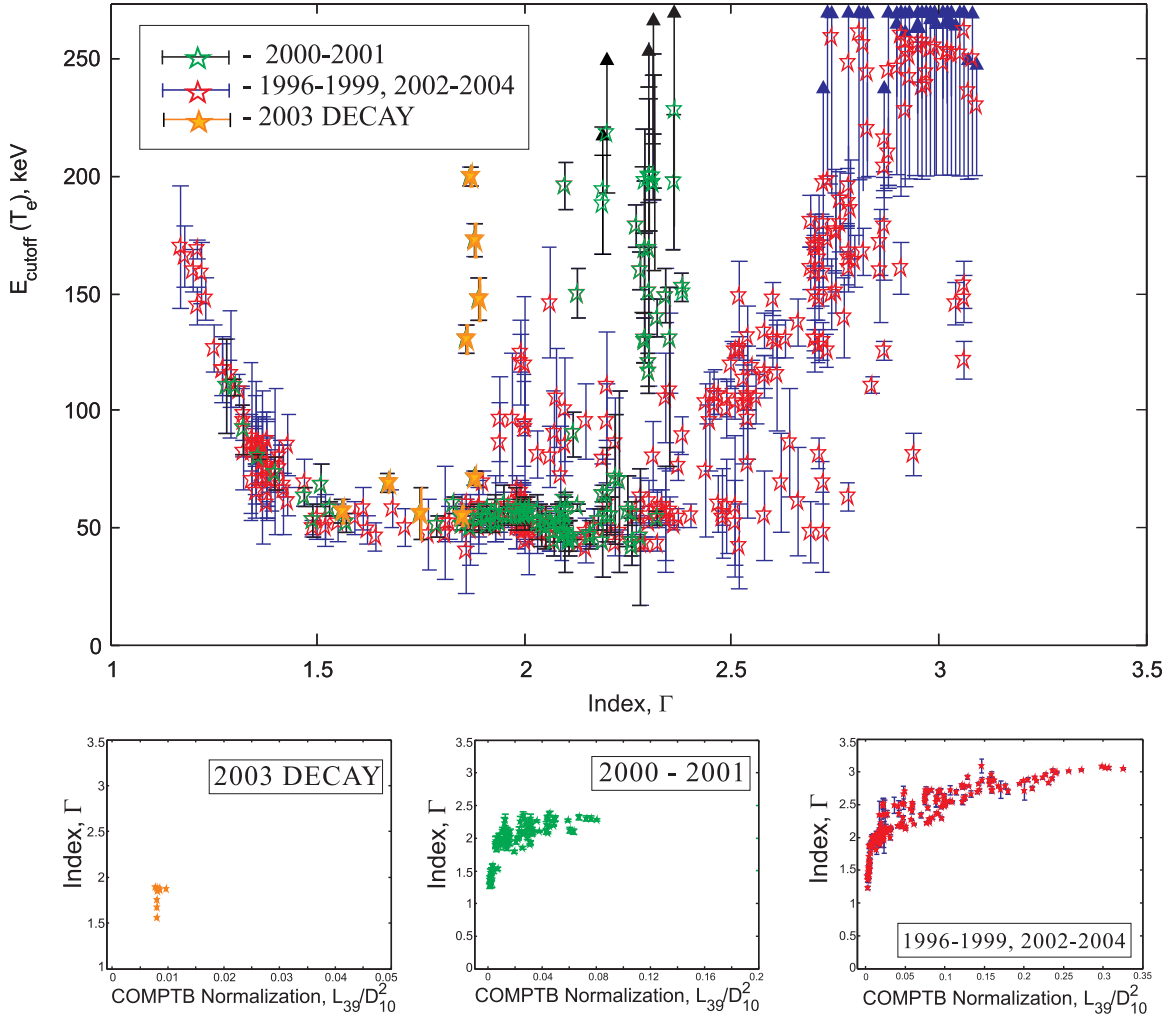
4U 1630-47

Figure 10. Top: cutoff energy E_{cutoff} vs. photon index Γ for *RXTE* observations of 4U 1630–47. Spectral parameters from 1996–1999 and 2002–2004/2000–2001/ 2003[decay] outburst sets are marked in red/green/yellow stars to indicate the saturation levels about $\Gamma \sim 3.0/2.3/1.9$, respectively. Bottom: Γ vs. *Comptb* normalization correlations for all indicated observations: decay 2003 (left), 2000–2001 (center), and 1996–1999 and 2002–2004 (right) outburst sets. Correlation shows three different tracks, which correspond to different index saturation levels. Index saturation level probably correlates with high-energy cutoff E_{cutoff} (see top panel and the text).

(A color version of this figure is available in the online journal.)

leading to strong radio emission (due to high radiation pressure; see an explanation of this effect in Titarchuk et al. 2007), and another one accretes through the disk into the BH.

Using *BeppoSAX* data and our model *wabs* ∗ (*Bbody* + *Comptb* + *Laor*), we identify a *blackbody* component that has the temperature $kT_{BB} \sim 0.6$–0.7 keV and the seed blackbody temperature $kT_s \sim 1.2$ keV. *RXTE* data show that kT_s varies in the 1.0–2.0 keV interval while kT_{BB} is fixed at 0.7 keV. These best-fit values of kT_s are different from those obtained by T05 using the same *RXTE* data (herein the R5 set). Namely, T05 find that kT_s changes in the 2.7–3.8 keV interval for about half of VHS spectra of 4U 1630–47, while the other half have these temperatures less than 1.8 keV for the model *wabs* ∗ (*diskbb* + *powerlaw*). Using the same spectral model, Trudolyubov et al. (2001) obtain kT_s in the range of 1.2–1.8 keV for the R2 set. This difference of the seed photon temperature values found by T05 and Trudolyubov et al. can be explained by particular properties of the spectra for R2 and R5 outbursts. However, we show, using our spectral model, that kT_s values are similar for all outbursts and change between 1 and 2 keV.

We can suggest that this difference between T05 and our results is possibly due to the different spectral models used.

6. CORRELATIONS BETWEEN SPECTRAL AND TIMING PROPERTIES DURING SPECTRAL STATE TRANSITIONS

The *RXTE* light curves have been analyzed using the FTOOLS *powspec* task. The timing analysis *RXTE*/PCA data were performed in the whole PCA energy range by combining the high time resolution *event* and *binned* data modes. We have generated PDSs in the 0.1–512 Hz frequency range with millisecond time resolution. We subtracted the noise contribution due to Poissonian statistics. To investigate the evolution of the source timing properties, we modeled the PDSs using analytic models and the χ^2 minimization technique in the framework of the QDP/PLT plotting package.[9]

The broadband power density spectrum of the source is commonly presented by the noise component, whose shape in

---

[9] http://heasarc.gsfc.nasa.gov/ftools/others/qdp/qdp.html

14
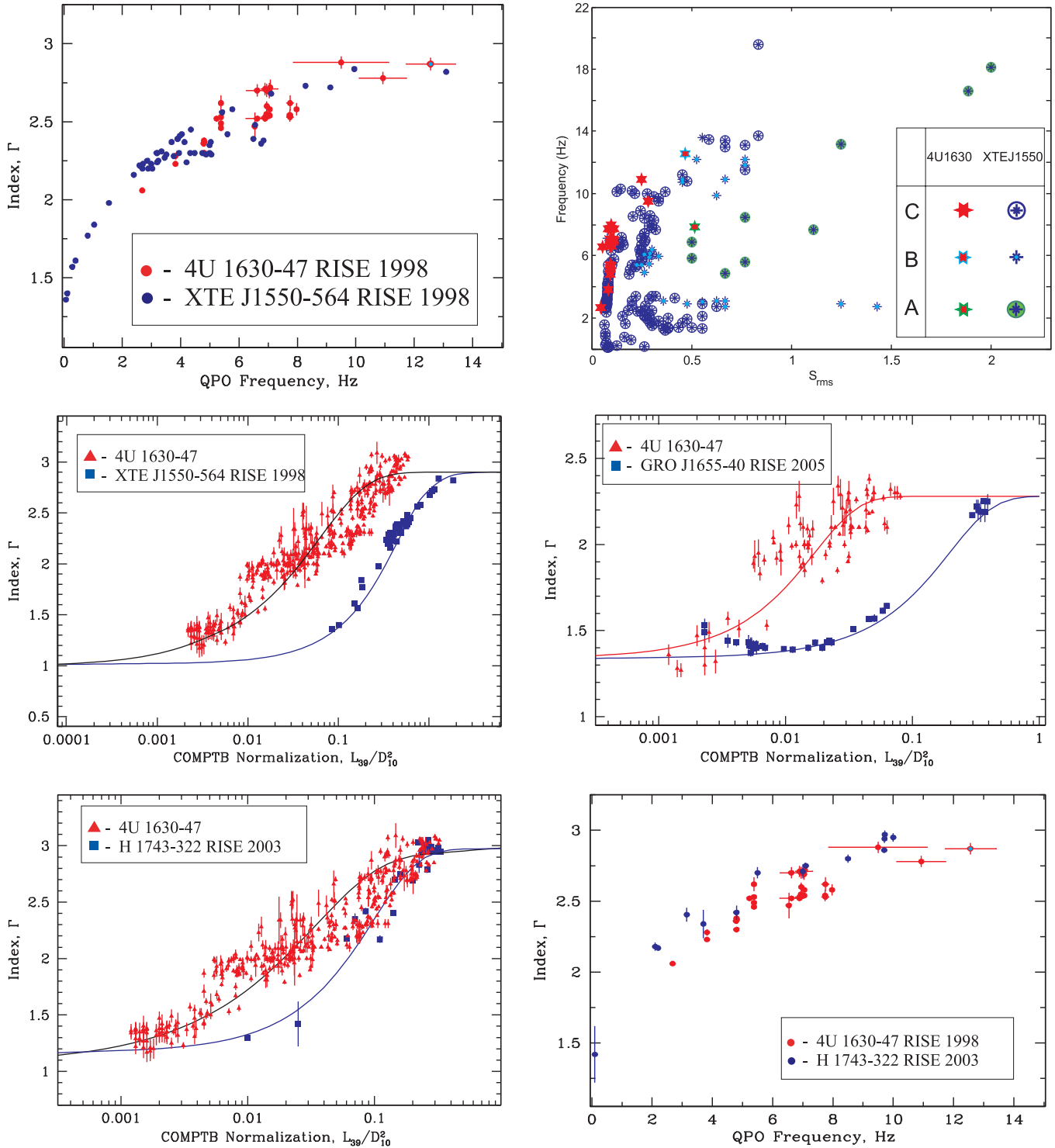
Figure 11. Scaling of photon index Γ for 4U 1630–47 (with red points for target source) and XTE J1550–564, GRO J1655–40, and H1743–322 (with blue marks for reference source). QPO frequency as a function of S_{rms} (the inverse of the rms) for two objects (4U 1630–47 and XTE J1550–564) is presented in the top right panel with the indications of the type A, B, and C QPOs.

(A color version of this figure is available in the online journal.)

the LHS and IS usually has a band-limited noise (BLN) profile approximated by an empirical model $P_X \sim [1.0 + (x/x_*)^2]^{-in}$ (the *KING* model in QDP/PLT). The parameter x_* is related to the break frequency, and $2 \cdot in$ is a slope of the PDS continuum after the break frequency x_*. In addition to the flat-top continuum in the LHS and the IS, PDS often shows QPOs, modeled by Lorentzians. In the HSS and VHS an additional

power-law component (very low frequency noise, VLFN) is needed to fit the data at the lowest frequencies.

In Figure 12 we show details of the evolution of X-ray timing and spectral characteristics for the 1998 *rise* transition (*R*2). At the top of this figure we show an evolution of the 1.3–12 keV ASM flux during this outburst. We choose representative observations designated by *red/blue* colors and
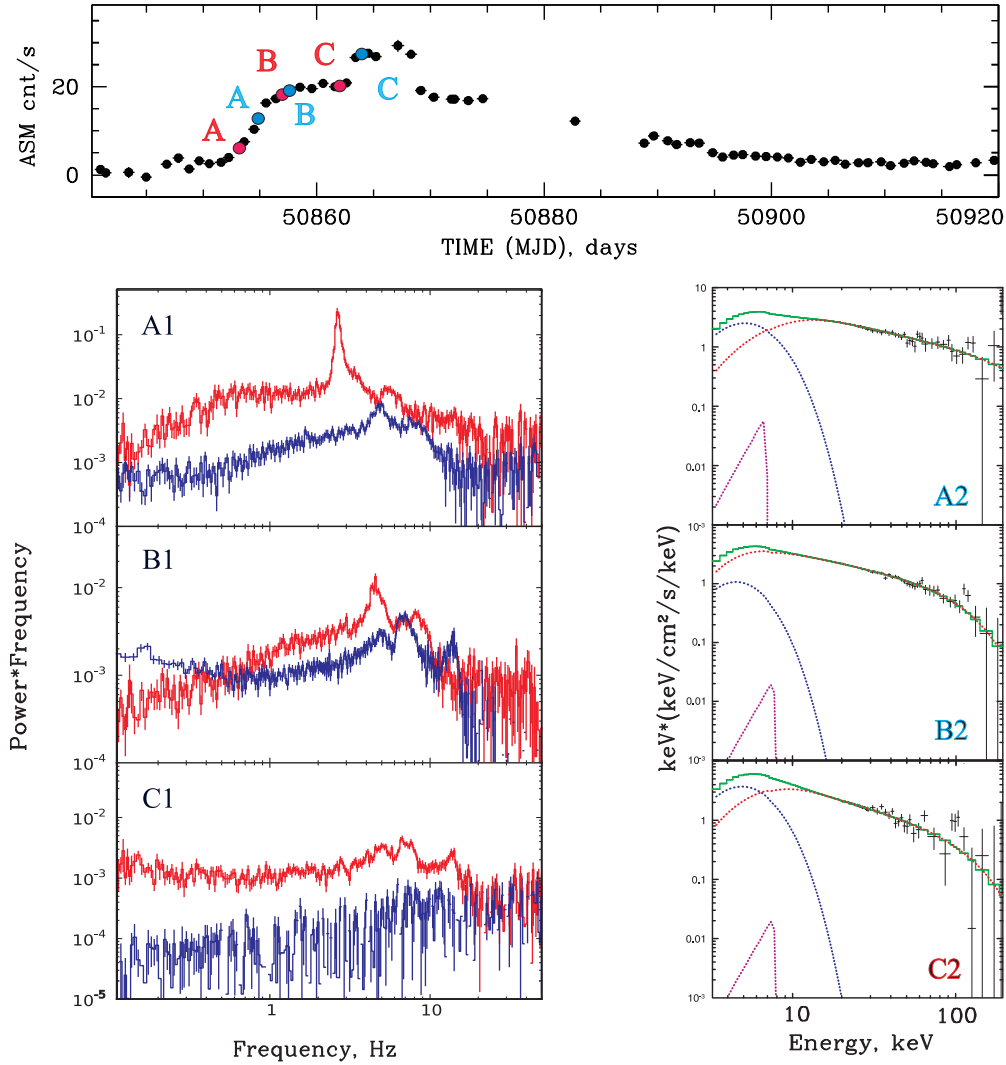
Figure 12. Top: evolution of the 1.3–12 keV ASM flux during the 1998 rise transition events ($R2$). Red/blue points A, B, and C mark moments at MJD = 50,853.1/ 50,855.8, 50,856.1/50,857.8, and 50,862.6/50,864.2, respectively. Bottom: PDSs for 3–13 keV band (left column) are plotted along with the $E * F(E)$ diagram (right column) for A, B, and C points of X-ray light curves. $E * F(E)$ diagrams (panels A2, B2, C2) are related to the corresponding power spectra for panels A1 (point A, blue), B1 (point B, blue), C1 (point C, red). The data are shown by black points, and the spectral model components are displayed by red, blue, and pink dashed lines for *Comptb*, *Blackbody*, and *Laor* components, respectively.

(A color version of this figure is available in the online journal.)

letters A, B, and C to demonstrate the PDS for six characteristic epochs at MJD = 50,853.1/50,855.8, 50,856.1/50,857.8, and 50,862.6/50,864.2, respectively, as shown on the ASM flux diagram at the top of Figure 12.

In the bottom left panel of Figure 12 we plot PDSs for three observations indicated as A, B, C moments, while the corresponding energy spectra in the form of the $E * F(E)$ diagram are shown in the bottom right panel. In the energy spectral diagrams the data points are shown by black lines, while the spectral model components are presented by *red*, *blue*, and *pink* dashed lines for *Comptb*, *Blackbody*, and *Laor*, components respectively.

Points A [*red* (30178-01-01-00) and *blue* (30178-01-03-00)] correspond to the IS, whereas points B and C [B *red* (30188-02-02-00), B *blue* (30178-02-02-00), C *red* (30178-01-10-00), C *blue* (30188-02-14-00)] are related to the VHS. All of these observations, except 30188-02-14-00 (C *blue*), exhibit power spectra with strong BLN accompanied by QPO peaks. Evolution of the temporal properties of the source during the *rise* phase of the 1998 outburst is characterized by a monotonic decrease

of the total rms amplitude (from 28% to 10%) and an increase of the BLN break and QPO centroid frequencies (from 2 Hz to 13 Hz). Note that during X-ray flux plateau intervals the source emission is also characterized by the stable spectral and timing parameters. The 1.3–12 keV flux rise is accompanied by a systematic shift of the frequency of maximum power in PDS toward higher frequencies (see corresponding PDS×frequency diagrams for A and B points).

The energy spectra shown in the right column (panels A2, B2, C2) are related to the corresponding power spectrum diagrams, for panels A1 (point A *blue*), B1 (point B *blue*), and C1 (point C *red*). $E * F(E)$ diagrams demonstrate an evolution of the spectral properties of 4U 1630–47 during the outburst rise phase, which is characterized by a monotonic steepening of the photon index Γ from 1.5 to 3 (see *red* points in Figure 13). Note that similar correlations were revealed in many X-ray BH binaries (e.g., ST09; TS09; TSA07; SBKM13). This simultaneous spectral and timing analysis shows that state transitions in 4U 1630–47 are in agreement with the *canonical* BH spectral state evolution (see, e.g., ST09). Namely, the correlation of the photon index
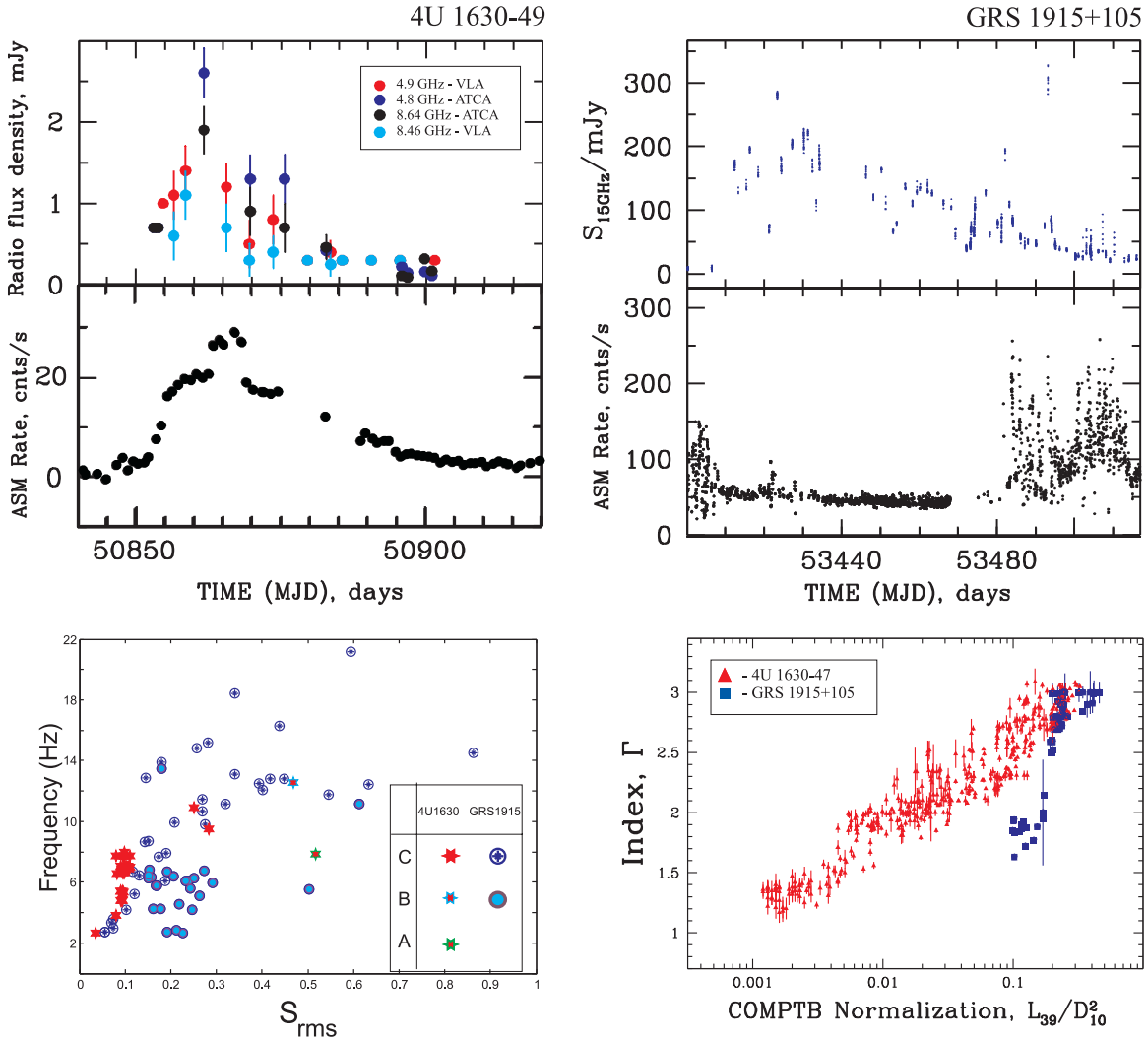
Figure 13. Top: evolution of flux density at 4.9 GHz (VLA, red), 4.8 GHz (ATCA, blue), 8.64 GHz (ATCA, blue), and 8.46 GHz (VLA, bright blue, taken from Hjellming et al. 1999) and *RXTE*/ASM count rate during 1998 outburst transition of 4U 1630–47 (left column) and evolution of flux density $S_{15\,GHz}$ at 15 GHz (Ryle Telescope, taken from TS09) and *RXTE*/ASM count rate during 2005 outburst transition (right column) of GRS 1915+105. Bottom: QPO frequency as a function of S_{rms} (the inverse of the rms) for 4U 1630–47 and GRS 1915+105 (taken from Soleri et al. 2008) is presented with the indications of the type A, B, and C QPOs (left). Right: photon index Γ vs. normalization for 4U 1630–47 (red points) and GRS 1915+105 (blue points for the 1997 outburst transition, taken from TS09).
(A color version of this figure is available in the online journal.)

Γ with the QPO frequencies (see, e.g., ST09; SBKM13; and the present work)) can be considered as observational evidence for the presence of the TL. In the framework of this scenario these QPOs are caused by oscillations in this bounded TL with frequencies equal to eigenfrequencies of the configuration. Any boundary configuration, in our case the TL or Compton cloud, is characterized by its own eigenfrequency. In order to observe this frequency, there should be enough power in excitation of this frequency. It is not by chance that we see these low-frequency QPOs situated very close to the break frequency in the power spectrum (for more details on the theory of oscillations of a bounded medium, see Landau & Lifshitz 1976; TSA07)

Consequently, this evolution of the QPO frequency can be interpreted as a change of the TL size, or the inner boundary of the Keplerian accretion disk where the disk starts to adjust to sub-Keplerian motion in the TL. Thus, the X-ray spectrum is formed in the relatively hot TL and evolves as a result of thermal and dynamical Compotonization of soft (disk) photons, and QPOs are seen as intrinsic oscillations of the TL zone.

While the exact nature of QPOs is under debate, the prediction of the TL oscillation interpretation that the QPO frequency

increases with the flux is confirmed by the observations. Moreover, the spectral index versus QPO correlation established for many BHC sources allows us to estimate the compact object masses in these sources, which we find to be consistent with mass function estimates (see ST09). We argue that that the observable correlations between spectral and timing characteristics seen in 4U 1630–47 are consistent with those obtained in other BHCs (see, e.g., ST09; SBKM13).

7. DISCUSSION

7.1. Saturation of the Index is a Possible Signature of a BH

In our analysis of the evolution of the photon index Γ in 4U 1630–47 using *RXTE* and *BeppoSAX* observations we have firmly established that the index saturates with the low-QPO frequency and probably with the *Comptb* normalization N_{com}, which is proportional to the (disk) mass accretion rate, $\dot{M}$ (see Figure 11). ST09 give strong arguments that this index saturation is a signature of converging flow onto a BH. In fact, the Comptonization spectral index is an inverse of a product of the number of scatterings N_{sc} and the efficiency of upscattering η.

In the converging flow N_{sc} is proportional to the mass accretion rate $\dot{M}$ and η is inversely proportional to $\dot{M}$ for $\dot{m} = \dot{M}/\dot{M}_{\rm Edd} \gg 1$, and thus one can expect the index saturation when $\dot{m} \gg 1$. In addition, we reveal that the index Γ correlates and saturates when QPO frequency increases. The index–QPO relation now established in many BHs strongly suggests that low-frequency QPOs are a result of an oscillatory process in the Compton cloud (TL).

Titarchuk et al. (1998) predicted that the TL should become more compact when mass accretion rate, $\dot{M}$, increases. For a BH case Laurent & Titarchuk (1999, 2011), hereafter LT99 and LT11, find, using Monte Carlo simulations, that the index should saturate when $\dot{M}$ increases. The photon index increase and subsequent saturation versus $\dot{M}$ were firmly established by ST09, TS09, and ST10, and we confirm this effect in the current work. In particular, as one can see in Figure 11, the values of Γ monotonically increase from 1.2 and finally saturate at a value about 3.

Thus, we argue that the X-ray observations of 4U 1630–47 reveal the index saturation versus mass accretion rate, which can be a signature of the converging flow (or a BH presence) in this source. The index−*Comptb* normalization (or $\dot{M}$) and the index–QPO correlations allow us to estimate a BH mass in 4U 1630–47 (see Figure 11 and Section 7.3 below) even without an observation of the optical counterpart of 4U 1630–47.

An additional argument in favor of a BH (or event horizon) presence is the observational fact that the cutoff energy of the spectra, $E_{\rm cutoff}$, has values about 200 keV (see the upper panel of Figure 10 and also Grove et al. 1998). It is interesting that a similar result was obtained by LT99 and LT11 using Monte Carlo simulations. They argue that for high mass accretion rates (exceeding the Eddington limit, $\dot{m} = \dot{M}/\dot{M}_{\rm Edd} > 1$) the cutoff energy is of the order of the electron rest mass, $E_{\rm cutoff} \sim a \cdot m_e c^2$, where $a \sim 0.5$–0.7. Thus, the case of $E_{\rm cutoff} \gtrsim 200$ keV indicates a significant effect of the bulk motion inflow, which, in turn, points to the presence of a BH event horizon.

We also find different spectral index saturation levels for different outbursts (see bottom panel of Figure 10). Furthermore, complex flaring events during the longest activity period, 2003 2004, exhibit a number of close but clearly separated levels. The 2003 outburst (MJD = 52,681.8 – 52,689.1) is characterized by a low saturation level of Γ (yellow stars in Figure 10). The index saturation value $\Gamma_{\rm sat}$ is probably related to a value of the converging inflow electron temperature kT_e. Namely, $\Gamma_{\rm sat}$ increases when kT_e decreases (see LT99; LT11). The same behavior was found by ST09 in XTE 1550–564 for multiple state transitions during the 1998 outburst.

7.2. On the Non-monotonic Behavior of the Cutoff Energy E_{cut} versus Index Γ

Our spectral analysis reveals a non-monotonic behavior of the cutoff energy $E_{\rm cutoff}$ versus index Γ (see Figure 10). In the upper panel of this figure we demonstrate how $E_{\rm cutoff}$ changes with Γ. At low values of the index ($\Gamma < 2$) the cutoff energy $E_{\rm cutoff}$ decreases and reaches its minimum in the 50–80 keV range. Then for $\Gamma \gtrsim 2$ the energy $E_{\rm cutoff}$ starts to increase again. Similar behavior of $E_{\rm cutoff}$ versus Γ was predicted by LT11 based on Monte Carlo simulations.

The $E_{\rm cut}$–Γ tracks during the 2000–2002 outbursts, at the 2003 decay, and during the 1996–1999 and 2002–2004 outbursts were different from each other (see Figure 10). Namely, the saturation levels for 2000–2001 and 2003 (*decay*) spectra were lower ($\Gamma \sim 2.3$–2.4 and $\Gamma \sim 1.8$, respectively) than

those for other spectra for which $\Gamma \sim 3$. It is interesting to note that the 2000–2001 data (green points) lie close to the 1996–1999 and 2002–2004 outburst data for LHS-IS transitions (red points). This indicates that during rise episodes similar accretion regimes are operating for all outbursts. Then, $E_{\rm cutoff}$ starts to increase and the index saturates at different values of $\Gamma_{\rm sat}$ for each of the outbursts: $\Gamma \sim 2.3$–2.4 (green stars for 2000–2001 outbursts), $\Gamma \sim 1.8$–1.9 (yellow stars for 2003 [*decay*] outburst), and $\Gamma \sim 2.8$–3 (red stars) for the remaining 1996–1999 and 2002–2004 outbursts (see Figure 10). According to the LT11 Monte Carlo simulations, different index saturation levels are caused by different values of the electron temperature kT_e, where higher $\Gamma_{\rm sat}$ correspond to the lower values of kT_e. In other words, at higher mass accretion rate the plasma temperature kT_e and consequently an efficiency of thermal Comptonization substantially decrease. In this case the bulk motion Comptonization dominates over the thermal one, forcing $E_{\rm cutoff}$ to be shifted to higher values.

The $E_{\rm cut}$–Γ dependence shown by 4U 1630–47 is strikingly similar to those discovered in GX 334–9 by Motta et al. (2009) and subsequently reported in XTE J1550–564 by Titarchuk & Shaposhnikov (2010). Especially remarkable is the resemblance of the $E_{\rm cut}$–Γ track shown in Figure 10 for 4U 1630–47 to that for XTE J1550–564 (see Figure 4 in Titarchuk & Shaposhnikov 2010). Therefore, the presented correlations between cutoff energy and index for 4U 1630–47 add yet another aspect of similarity of this source with other BHC sources.

7.3. Determination of BH Mass in 4U 1630–47

In this section we apply the scaling technique developed in ST07 and ST09 to make a BH mass estimate for 4U 1630–47 based on X-ray data. Note that BH mass evaluation for this object is impossible by any traditional dynamical methods based on optical data because of large visual extinction toward the source.

We carry out a scaling analysis of 4U 1630–47 with a number of sources such as XTE J1550–564, H1743–322, and GRO J1655–40 to give cross-check results. It is worth noting that we can proceed with this scaling technique if the correlations between these particular sources are self-similar. In other words, we implement this scaling technique when the given correlations have (1) the saturation part at high Γ level of the corresponding track, (2) the same index saturation levels, and (3) the same slopes as an index function of QPO frequency.

7.3.1. Scaling of 4U 1630–47 with XTE J1550–564

[stop] The X-ray nova XTE J1550–564 is a well-studied BHC X-ray binary with one of the best measured mass and distance among known stellar mass BH sources (see Table 5). Note that the scaling between 4U 1630–47 and XTE J1550–564 can be implemented using 1998 rise outburst data of XTE J1550–564 observed with *RXTE*. This 1998 rise outburst was previously discussed in detail by many authors (see, e.g., Remillard et al. 2002, hereafter R02; and ST09). R02 and ST09 implemented a deep timing and spectral analysis for *RXTE* data collected during the rise outburst (time) interval from 1998 September 8 to 1998 October 16 (MJD 51,069–51,105). R02 found the C-type LFQPOs in the power spectra and investigated the behavior of QPO frequency as a function of the total rms amplitude. Casella et al. (2005) noted that all these A-, B-, and C-type QPOs, in particular, for XTE J1550–564, form the corresponding tracks at proper areas in the diagram of QPO frequency versus the

Table 5
BH Masses, Distances, and Inclination Angle Determination

Source	$M_{\rm dyn}$[a] $(M_\odot)$	$i_{\rm orb}$[a] (deg)	d[a] (kpc)	$i_{\rm scal}$[a] (deg)	$M_{\rm scal}$ $(M_\odot)$	Refs.
XTE J1550–564	9.5 ± 1.1	72 ± 5	~ 6	$\cdots$	10.7 ± 1.5[c]	1, 2, 3
GRO J1655–40	6.3 ± 0.3	70 ± 1	3.2 ± 0.2	$\cdots$	$\cdots$	4, 5
H1743–322	~ 11	~ 70	~ 10	$\cdots$	13.3 ± 3.2[c]	6
GRS 1915+105	14 ± 4	~ 60	12.1 ± 0.8	$\cdots$	15.6 ± 1.5[d]	4, 7
4U 1630–47	$\cdots$	$\cdots$	~ 10	$\leqslant 70$	9.5 ± 1.1	this work

Notes.
[a] Dynamically determined BH mass and system inclination angle.
[b] Source distance found in literature.
[c] Scaling value found by ST09.
[d] Scaling value found by ST07.
References. (1) Orosz et al. 2002; (2) Sánchez-Fernández et al. 1999; (3) Sobczak et al. 1999; (4) Greene et al. 2001; (5) Hjellming & Rupen 1995; (6) McClintock et al. 2007; (7) ST09.

inverse of the rms (hereafter $S_{\rm rms}$; see top panel on the right column of Figure 11).

ST09 revealed a change of the photon index Γ from 1.4 to 2.9 in the X-ray spectra of XTE J1550–564. Γ increases when the C-type LFQPO increases, forming a characteristic correlation having the saturation part at high value (8–13 Hz) of LFQPO (ST09; see also the top panel on the left column of Figure 11) with $\Gamma_{\rm sat} \sim 3$. It is interesting that the spectral index also shows a positive correlation with the *normalization* parameter (proportional to mass accretion rate) along with the saturation plateau at the same level $\Gamma_{\rm sat} \sim 3$ at high values of the *normalization* parameter. This behavior of XTE J1550–564 during outburst rise is similar to the evolution of spectral and timing parameters of 4U 1630–47 in terms of Γ–Norm and Γ–LFQPO diagrams. The saturation levels and the slopes of corresponding correlation tracks as a function of QPO frequency and the spectral normalization are the same (see top and middle panels of the left column in Figure 11).

In order to proceed with the scaling procedure, we parameterize the correlation pattern Γ–Norm/ Γ–QPO frequency for a reference transition in terms of the analytical function

$$F(x) = A - (D \cdot B)\ln\{\exp[(1.0 - (N/N_{tr})^\beta))/D] + 1\}. \quad (1)$$

By fitting this functional expression to the correlation pattern, we find a set of parameters A, B, D, N_{tr}, and β that represent a best-fit form of the function $F(x)$ for a particular correlation curve. For $N \gg N_{tr}$, the correlation function $F(x)$ converges to a constant value A. Consequently, A is the value of the index saturation level, β is the power-law index of the inclined part of the curve, and N_{tr} is the value at which the index transitions, i.e., levels offset. Parameter D determines how smoothly the fitted function saturates to A. We scale the data to a template by applying a transform $N \rightarrow s_N \times N$ until the best fit is found.

XTE J1550–564, has a reliable dynamical mass determination of $9.5 \pm 1.1\,M_\odot$, (Orosz et al. 2002), which corroborates our scaling method which gives the value of $10.7 \pm 1.5\,M_\odot$ (see ST09). We use the Γ–Norm correlation and the scaling BH mass as reference data in our subsequent analysis. The reference data set is well represented by the function defined in Equation (1). We fit $F(x)$ to best represent the XTE J1550–564 Γ–Norm track, varying the parameters A, N_{tr}, and β. To test for self-consistency, we have used the chi-squared statistical minimization method to determine the best-fit parameter values. Parameters D and B are not well constrained by the data. Therefore, we fix those parameters at 1.0 and 0.6, respectively, based

on our previous experience with correlation parameterization (Table 4 of ST09). The best-fit approximations by the analytical function (Equation (1)) are presented in Figure 11 along with observational data. As a result, for free parameters we obtain the following best-fit values: $A = 2.94 \pm 0.08$ (saturation level), $N_{tr} = 0.011 \pm 0.004$, $\beta = 0.99 \pm 0.14$. We then obtain the *first* scale factor $s_N = 2.2 \pm 0.5$.

The *second* scaling factor s_ν follows from the scaling law

$$s_\nu = \frac{\nu_r}{\nu_t} = \frac{M_t}{M_r}, \quad (2)$$

which is based on the inverse dependence of the QPO frequencies on BH mass in terms of the TL model (see details in TLM98; TF04; Appendix A of ST09) using the scaling of the photon index versus QPO frequency correlation. Here M_r is BH mass of the reference source (XTE J1550–564), and M_t is BH mass of the target source (4U 1630–47). Subscripts r and t of frequency ν denote the reference and target sources, respectively.

As is seen from Figure 11 (top left panel), the index–QPO frequency diagram for 4U 1630–47 (blue points) follows that for XTE J1550–564 (red points). Thus, the index–QPO frequency diagrams for both sources are nearly equivalent. In this way, one obtains that the scaling factor $s_\nu = 1.00 \pm 0.01$ and the mass of target source (4U 1630–47) using Equation (2) is $M_t = s_\nu M_r$. Assuming the mass estimate of $9.5 \pm 1.1\,M_\odot$ (Orosz et al. 2002), we estimate a BH mass for 4U 1630–47 (see Table 5).

Note that the Γ–QPO correlation is independent of the distances and the geometrical factors such as an inclination angle (see Equation (2)), while the Γ–Norm correlation is closely related to these parameters. Thus, using the mass estimate $9.5 \pm 1.1\,M_\odot$ for 4U 1630–47, we have an opportunity to evaluate the inclination angle for this source 4U 1630–47 using the Γ–Norm scaling.

According to the scaling laws (see Equations (8) and (9) in ST09), the expression for the geometrical factor f_G in 4U 1630–47 is

$$f_G = s_N \frac{M_t d_r^2}{M_r d_t^2}, \quad (3)$$

where geometric factor, by definition (ST09), $f_G = (\cos\theta)_r/(\cos\theta)_t$, inclination angles θ_r, θ_t, and d_r, d_t are distances to the reference and target sources. Furthermore, if we know mass M_t (see Equation (2)) and the *first* scaling index s_N, we can find an inclination angle θ_t for the target source 4U 1630–47 using a formula for $f_G = (\cos\theta)_r/(\cos\theta)_t$ and

values of parameters (θ_r and d_r) for XTE J1550–564

$$(\cos\theta)_t \sim \frac{(\cos\theta)_r}{s_\nu s_N} \times \left(\frac{d_t}{d_r}\right)^2. \qquad (4)$$

We show the estimated values of BH mass and the inclination angle with the proper error bars for the target source (4U1630–47) along with parameters for the reference source (XTE J1550–564) in Table 5.

It is interesting that there are many indications obtained by other methods in favor of a high inclination value for the binary 4U 1630–47. Recently, Muñoz-Darias et al. (2013) gave clear indications on a high inclination of 4U 1630 based on the *RXTE* observations during outburst transitions. They find significant difference between the shape of the tracks that high-inclination systems display in the color/luminosity diagrams and that of low-inclination systems.

Note that the derived estimate of the inclination angle $\theta \lesssim 70°$ in 4U 1630–47 predicts that deep orbital eclipses should be absent. In fact, X-ray observations of the source do not show any strictly recurrent dip events. However, this does not exclude a possibility of partial orbital eclipses. Furthermore, the presence of a wind from the accretion disk can result in an absorption of the X-ray emergent radiation due to a high optical depth in a wind envelope. This picture is consistent with an absorption-line detection in X-ray high-resolution spectra of 4U 1630–47 with *Suzaku* (Kubota et al. 2007) who find that these X-ray spectra reveal strong absorption lines from highly ionized (H-like and He-like) iron K_α at 7.0 keV and 6.7 keV. A possible origin of these lines can be associated with an outer part of the accretion disk.

A number of X-ray binaries have been found to show that absorption lines originated from highly ionized elements. (Boirin et al. 2004). These types of sources range from microquasars, e.g., GRO J1655–40 (e.g., Miller et al. 2006; Yamaoka et al. 2001; Ueda et al. 1998), to low-mass X-ray binaries, e.g., GX 13+1 (Sidoli et al. 2002; Ueda et al. 2004). All of them are viewed at high inclination angles.

In addition, the detection of a dip in the X-ray light curve of 4U 1630–47 during the 1996 outburst (see Kuulkers et al. 1998) indicates that the inclination of the system is fairly high, which is similar to GRO J1655–40. This single dip (140 s of time duration) during the 1996 outburst (Kuulkers 1998) could be caused by inner conditions such as the attenuation (screening) of the X-ray region by inner structures of the accretion disk, a sporadic (irregular) absorption of the clumping in the wind, high current inclination due to disk precession, and so on. However, after the 1996 outburst no more similar dips were detected.

One can conclude that the detection of a single isolated dip (possibly partial orbital eclipse) in the 1996 outburst can indicate a high orbital inclination angle ($\theta \leqslant 75°$). On the other hand, the inclination angle is not sufficiently high because the regular eclipses are not observed. This imposes a constraint on the inclination angle $\theta \lesssim 70°$.

7.3.2. Scaling of 4U 1630–47 with H1743–322

For an additional cross-check of the mass evaluation of $\sim 10\ M_\odot$ for BH mass in 4U 1630 we use another object, H1743–322. Note that the Γ–QPO and Γ–normalization correlation curves for the 2003 rise data of H1743–322 (taken from ST09) are self-similar with correlations that we derive for 4U 1630–47 (see Figure 11). The 2003 outburst in H1743–322 was detected on March 21 in hard X-rays (15–200 keV) by

INTEGRAL (IGR J17464–3213; Revnivtsev et al. 2003). Follow-up observations with *RXTE* led to the recognition that this source is a recurrent X-ray nova that was first observed with the Ariel V All-Sky Monitor by Kaluzienski & Holt (1977). Further, the X-ray spectral and temporal properties of X-ray data, as well as radio detection of large-scale relativistic X-ray jets (Corbel et al. 2005), allow us to classify H1743–322 as a BHC (Fender 2006). A transient X-ray system H1743–322 is a source of X-ray, radio, optical, and near-infrared emissions, which enable one to evaluate its parameters such as the distance, orbital inclination, and BH mass (McClintock et al. 2007).

As is seen from Table 5, H1743–322 is characterized by almost the same BH mass as that for 4U 1630–47 (based on the mass determination by the scaling with XTE J1550–564; see the previous section). Indeed, H1743–322 and 4U 1630–47 demonstrate a similar index saturation level and Γ–QPO correlations. (see Figure 11). Considering a BH mass for H1743–322 of $M_{H1743} \sim 10\ M_\odot$, we can also confirm our BH mass estimate $\sim 10\ M_\odot$ for 4U 1630–47.

Moreover, these two sources have the same geometrical parameters (distances and inclination angles). In this case their Γ–Norm tracks should also resemble each other. As seen from Figure 11, the correlation tracks for both objects are similar, showing the same saturation levels. However, the Γ–Norm correlation for H1743–322 is located to the right from that for 4U 1630–47. We apply Equation (2) to Γ–QPO correlations for 4U 1630–47 and H1743–322 (bottom right panel of Figure 11) to obtain $s_\nu = 0.85 \pm 0.08$. We thus estimate that $M_{1630} = 9.80 \pm 0.08\ M_\odot$. We can also estimate $M_{BH} = 9.6 \pm 0.1\ M_\odot$ in 4U 1630–47 using Γ–Norm correlations (bottom left panel of Figure 11) if we use M_r ($M_{1743} = 11.5\ M_\odot$; McClintock et al. 2007) for the reference source in Equation (3) assuming $f_G = 1$ (namely, inclinations for both objects are the same, ~ 70 degrees), $s_N = 1.2 \pm 0.1$, $D_{1630} = 10$ kpc, $D_{1743} = 10$ kpc.

Note that spectral and temporal evolution of H1743–322 is similar to that observed in XTE J1550–564 during 1998–1999 (Sobczak et al. 2000; RM06) and in GRO J1655–40 during 1996–1997 (Sobczak et al. 1999; Remillard et al. 2002; RM06).

7.3.3. Scaling of 4U 1630–47 with GRO J1655–40

The photon index Γ for 4U 1630–47 during the 2000–2001 period demonstrates a lower saturation level as a function of the normalization parameter (which is proportional to the mass accretion rate in the disk), namely, $\Gamma_{sat} \sim 2.5$. We can also make a BH mass estimate for 4U 1630–47 in the case of $\Gamma_{sat} \sim 2.5$. We choose scaling of the index–normalization previously found in GRO J1655–40 (see ST09) with that in 4U 1630–47 (see Figure 11, middle right panel).

The soft X-ray transient GRO J1655–40, Nova Sco 1994, is a well-studied BHC X-ray binary with the best measured mass and distance (Hjellming & Rupen et al. 1995; Greene et al. 2001; see Table 5). Note that the correlations between 4U 1630–47 and GRO J1655–40 are self-similar for the 2000–2001 and rise 2005 periods, respectively.

Thus, using Equation (3), we obtain that $M_{1630} \sim 10\ M_\odot$ ($M_{1630} = M_t$) if $f_G = 1$ (inclinations for both objects are the same, namely, ~ 70 degrees), $s_N = 6.00 \pm 0.08$, $D_{1630} = 10$ kpc, $D_{1655} = 3.2$ kpc, $M_{1655} = 6.3 \pm 0.3\ M_\odot$ ($M_{1655} = M_r$).

We want to emphasize that scaling of the correlations in 4U 1630–47 with that in XTE J1550–564, H1743–322, and GRO J1655–40 gives similar values of BH mass, about 10 solar masses for 4U 1630–47.

7.4. Comparison between 4U 1630–47 and GRS 1915–105

BHC binaries 4U 1630–47 and GRS 1915–105 demonstrate a number of similar spectral and timing properties, however we also would like to point out some significant differences between these objects. As a main similar signature in these objects, one can consider the same index saturation levels ($\Gamma_{\rm sat} \sim 3$) and the presence of LFQPOs in the power spectra for both objects, which are classified as the type B and C QPOs. Furthermore, the properties of these QPOs are the same in terms of the frequency-$S_{\rm rms}$ (the inverse of rms) diagram with very similar tracks for both objects (see bottom left panel of Figure 13). Despite showing the same saturation levels of the index correlation with the normalization in GRS 1915+105 and 4U 1630–47, these correlations are not self-similar (see the bottom right panel in Figure 13), and we cannot estimate BH mass in 4U 1630–47 using scaling with GRS 1915+105. Specifically, the index–normalization diagrams have different shapes: GRS 1915+105 is characterized by a stepper gradient of the index versus the normalization parameter than that for 4U 1630–47. In fact, 4U 1630–47 shows a lower level of the index range ($\Gamma_{\rm min,1630} < 1.5$) than that in GRS 1915+105, where the index Γ never reaches the *canonical* LHS value, $\Gamma_{\rm min,1915} > 1.5$ (see, e.g., Fender et al. 2004).

We should also point to different patterns in the radio/X-ray behavior for these objects. Namely, when we compare radio loud phases [at MJD = 50855–50865 for 4U 1630–47, see Figure 13 (top left panel) and MJD = 50910–51000 for GRS 1915+105, see top right panel there with the almost constant X-ray flux (so called "*plateau*" states). The peak of radio emission in GRS 1915 at 15 GHz, occurs at relatively low X-ray count rate (Soleri et al. 2008) while the peak of radio emission (4–9 GHz), in 4U 1630–47 is directly related to maximal X-ray count rate (Hjellming et al. 1999).

Note also that these objects sometimes demonstrate properties that are difficult to classify in terms of the canonical spectral states (McClintock & Remillard 2003). Some *anomalous* properties are similar for both objects. In particular, during the 1998 outburst rise 4U 1630–47 demonstrated an interesting phase that could be considered as a transition between the LHS and the VHS. On the other hand, the energy spectrum of the source was typically hard, with a well-determined exponential high-energy cutoff, similar to that in the low state. But the source power spectrum was typical for the very high state. Previously, Tomsick et al. (2005) also revealed a similar *anomalous* state in 4U 1630–47, which also revealed a disagreement between spectral and timing properties. Specifically, in the LHS during 2003–2004 *RXTE* observations 4U 1630–47 showed spectra typical for the LHS, while the corresponding power spectra contain strong BLN that is rather typical to the HSS. Note also that no radio detections during the 2002–2004 period were reported for 4U 1630–47. All these cases are not consistent with the *canonical* spectral state sequence and indicate the modified spectral state transition track for 4U 1630–47. It should be also noted that similar energy spectra related to the aforementioned timing behavior were observed at the low-luminosity state of GRS 1915+105 (Trudolyubov et al. 1999), during the rise phase in X-ray nova KS 1730–312 (Trudolyubov et al. 1996), and in GS/GRS 1124268 (Ebisawa et al. 1994).

There is also a striking resemblance between the X-ray properties of 4U 1630–47 during the rise of the 1998 outburst and GRS 1915+105 in the LHS (see Trudolyubov et al. 1999; TS09) and the *flaring* stage in the VHS (Tomsick et al. 2005). Moreover, radio observations of 4U 1630–47 with the ATCA

in 1998 during the brightest phase provide a detection of 28% and 26% linear polarization at 4.80 and 8.64 GHz, respectively (Hjellming et al. 1999). The large linear polarization can indicate optically thin jet ejections in 4U 1630–47. The above similarity of X-ray spectra of 4U 1630–47 and GRS 1915 supports the idea that 4U 1630–47 is also a relativistic jet source.

8. CONCLUSIONS

We present analysis of the X-ray spectral and timing properties observed from BHC X-ray binary 4U 1630–47 during transitions between the hard and soft states. We analyze several outbursts from this source observed with *BeppoSAX* and We apply the scaling technique to correlations of the photon index of the Comptonized component versus an LFQPO and versus the mass accretion rate. We interpret the changes of the spectral states in 4U 1630–47 in terms of a dynamical evolution of the Compton cloud.

We show that the X-ray broadband energy spectra of 4U 1630–47 during all spectral states can be modeled by a combination of a thermal component, a Comptonized component, and a red-skewed iron-line component. For our analysis we utilized the broad spectral coverage and resolution of *BeppoSAX* detectors from 0.3 to 200 keV along with frequent monitoring and outstanding time resolution of *RXTE* observations in the energy range from 3 to 200 keV.

In this work we present arguments for the presence of a BH in 4U 1630–47 based on the detailed analysis of X-ray spectral evolution in this source. We establish that the index monotonically increases during spectral transition from the low-hard state to the high-soft state and then finally saturates with the *Comptb* spectral normalization $N_{\rm com}(\propto \dot{M})$.

Moreover, the photon index saturates with $\dot{M}$ at several different levels for different outbursts. In the case when the photon index Γ saturates with $\dot{M}$ at the value of 3, we also find a correlation between Γ and the centroid of LFQPOs. ST09 give strong arguments that this index saturation is a signature of converging flow into a BH. It is important to note that the index monotonic growth and saturation at high mass accretion rates during transition from the low-hard to high-soft states have been recently demonstrated for many other BHC sources: GX 339–4, GRO J1655–40, XTE J1650–500, 4U 1543–47, XTE J1550–564, H1743–322, XTE J1859+226 (ST09), GRS 1915+105 (TS09), SS 433 (ST10). In view of these results, we thus suggest the presence of a BH in 4U 1630–47.

We also find that the Comptonized fraction f spans a wide range from 0.05 to 1, which points to variable X-ray illumination of the Compton cloud in 4U 1630–47 during state transitions. Furthermore, we argue that the changes of f are related to state transitions, which are presumably governed by the mass accretion regime.

Correlations between spectral and timing properties allow us to estimate a BH mass in 4U 1630–47 that is around 10 solar masses and the inclination angle $i \lesssim 70°$ applying the scaling method and using BHC XTE J 1550–564 as the reference source.

REFERENCES

Augusteijn, T., Kuulkers, E., & van Kerkwijk, M. H. 2001, A&A, 375, 447
Basko, M. M., Sunyaev, R. A., & Titarchuk, L. G. 1974, A&A, 31, 249

Belloni, T., Homan, J., Casella, P., et al. 2005, A&A, 440, 207
Belloni, T., Mendez, M., van der Klis, M., Lewin, W. H. G., & Dieters, S. 1999, ApJL, 519, L159
Boella, G., Chiappetti, L., Conti, G., et al. 1997, A&AS, 122, 327
Boirin, L., Parmar, A. N., Barret, D., Paltani, S., & Grindlay, J. E. 2004, A&A, 418, 1061
Bradt, H. V., Rothschild, R. E., & Swank, J. H. 1993, A&AS, 97, 355
Callanan, P. J., McCarthy, J. F., & Garcia, M. R. 2000, A&A, 355, 1049
Casella, P., Belloni, T., & Stella, L. 2005, ApJ, 629, 403
Chen, W., Shrader, C. R., & Livio, M. 1997, ApJ, 491, 312
Corbel, S., Aussel, H., Broderick, J. W., et al. 2013, MNRAS, 431, L107
Corbel, S., Kaaret, P., Fender, R. P., et al. 2005, ApJ, 632, 504
Cui, W., Chen, W., & Zhang, S. 2000, ApJ, 529, 952
Cui, W., Ebisawa, K., Dotani, T., & Kubota, A. 1998, ApJL, 493, L75
Dìaz, T. M., Miller-Jones, J. C. A., Migliari, S., Broderick, J. W., & Tzioumis, T. 2013, Natur, 504, 260
Dieters, S. W., Belloni, T., Kuulkers, E., et al. 2000, ApJ, 538, 307
Dieters, S. W., & van der Klis, M. 2000, MNRAS, 311, 201
Ebisawa, K., Ogawa, M., Aoki, T., et al. 1994, PASJ, 46, 375
Farinelli, R., & Titarchuk, L. 2011, A&A, 525, A102
Farinelli, R., Titarchuk, L., Paizis, A., & Frontera, F. 2008, ApJ, 680, 602 (F08)
Fender, R. P. 2006, in Compact Stellar X-Ray Sources, ed. W. Lewin & M. van der Klis (Cambridge: Cambridge Univ. Press), 381
Fender, R. P., Belloni, T. M., & Gallo, E. 2004, MNRAS, 355, 1105
Frontera, F., Costa, E., dal Fiume, D., et al. 1997, Proc. SPIE, 3114, 206
Giacchè, S., Gilli, R., & Titarchuk, L. 2014, A&A, 562, A44
Greene, J., Bailyn, C. D., & Orosz, J. A. 2001, ApJ, 554, 1290
Grindlay, J., Miller, G. F., & Tang, S. 2014, BAAS, 223, 406.06
Grove, J. E., Johnson, W. N., Kroeger, R. A., et al. 1998, ApJ, 500, 899
Hjellming, R. M., & Rupen, M. P. 1995, Natur, 375, 464
Hjellming, R. M., Rupen, M. P., Mioduszewski, A. J., et al. 1999, ApJ, 514, 383
Homan, J., & Belloni, T. 2005, Ap&SS, 300, 107
Homan, J., & Wijnands, R. 2002, ATel, 109, 1
Homan, J., Wijnands, R., van der Klis, M., et al. 2001, ApJS, 132, 377
Jones, C., Forman, W., & Tananbaum, H. 1976, ApJL, 210, L9
Kaluzienski, L. J., & Holt, S. S. 1977, IAUC, 3099, 3
Kerr, F. J., Bowers, P. F., Jackson, P. D., & Kerr, M. 1986, A&AS, 66, 373
Klein-Wolt, M., & van der Klis, M. 2008, ApJ, 675, 1407
Koljonen, K. I. I., McCollough, M. L., Hannikainen, D. C., & Droulans, R. 2013, MNRAS, 429, 1173
Kubota, A., Dotani, T., Cottam, J., et al. 2007, PASJ, 59, 185
Kuulkers, E. 1998, NewAR, 42, 1
Kuulkers, E., Parmar, A. N., Kitamoto, S., Cominsky, L. R., & Sood, R. K. 1997, MNRAS, 291, 81
Kuulkers, E., Wijnands, R., Belloni, T., et al. 1998, ApJ, 494, 753
Landau, L. D., & Lifshitz, E. M. 1976, Mechanics, Volume 1 (3rd ed.; Course of Theoretical Physics; Oxford: Elsevier Butterworth-Heinemann)
Laor, A. 1991, ApJ, 376, 90
Laurent, P., & Titarchuk, L. 1999, ApJ, 511, 289 (LT99)
Laurent, P., & Titarchuk, L. 2007, ApJ, 656, 1056 (LT07)
Laurent, P., & Titarchuk, L. 2011, ApJ, 727, 34
Levine, A. H., Bradt, H., Chakrabarty, D., et al. 1996, IAUC, 6390, 2
Lewin, W. H. G., van Paradijs, J., & Taam, R. E. 1997, in X-Ray Binaries, ed. W. H. G. Lewin, J. van Paradijs, & E. P. J. van den Heuvel (Cambridge: Cambridge Univ. Press), 175
Marshall, F. E. 1996, IAUC, 6389, 1
McClintock, J., & Remillard, R. 2003, in Compact Stellar X-Ray Sources, ed. W. H. G. Lewin & M. van der Klis (Cambridge: Cambridge Univ. Press), preprint (astro-ph/0306213)
McClintock, J. E., Remillard, R. A., Rupen, M. P., et al. 2007, arXiv:0705.1034
Miller, J., et al. 2006, BAAS, 38, 361
Mineo, T., Massaro, E., D'Ai, A., et al. 2012, A&A, 537, 18
Mitsuda, K., Inoue, H., Koyama, K., et al. 1984, PASJ, 36, 741
Motta, S., Belloni, T., & Homan, J. 2009, MNRAS, 400, 1603
Muñoz-Darias, T., Coriat, M., Plant, D. S., et al. 2013, MNRAS, 432, 1330

Oosterbroek, T., Parmar, A. N., Kuulkers, E., et al. 1998, A&A, 340, 431
Orosz, J. A. 2003, in IAU Symp. 212, A Massive Star Odyssey: From Main Sequence to Supernova, ed. K. van der Hucht, A. Herrero, & C. Esteban (San Francisco, CA: ASP), 365
Orosz, J. A., Groot, P. J., van der Klis, M., et al. 2002, ApJ, 568, 84
Parmar, A. N., Angelini, L., & White, N. E. 1995, ApJL, 452, L129
Parmar, A. N., Stella, L., & White, N. E. 1986, ApJ, 304, 664
Parmar, A. N., Williams, O. R., Kuulkers, E., Angelini, L., & White, N. E. 1997, A&A, 319, 855
Ponti, G., Fender, R. P., Begelman, M. C., et al. 2012, MNRAS, 422, L11
Priedhorsky, W. 1986, Ap&SS, 126, 89
Remillard, R. A., & McClintock, J. E. 2006, ARA&A, 44, 49 (RM06)
Remillard, R. A., Sobczak, G. J., Muno, M. P., & McClintock, J. E. 2002, ApJ, 564, 962
Revnivtsev, M., Chernyakova, M., Westergaard, N. J., et al. 2003, ATel, 132, 1
Sánchez-Fernández, C., Castro-Tirado, A. J., Duerbeck, H. W., et al. 1999, A&A, 348, L9
Seifina, E., & Titarchuk, L. 2010, ApJ, 722, 586 (ST10)
Seifina, E., & Titarchuk, L. 2011, ApJ, 737, 128
Seifina, E., & Titarchuk, L. 2012, ApJ, 747, 99
Seifina, E., Titarchuk, L., & Frontera, F. 2013, ApJ, 766, 63
Shakura, N. I., & Sunyaev, R. A. 1973, A&A, 24, 337
Shaposhnikov, N., & Titarchuk, L. 2007, ApJ, 663, 449 (ST07)
Shaposhnikov, N., & Titarchuk, L. 2009, ApJ, 699, 453 (ST09)
Shrader, C. R., Titarchuk, L., & Shaposhnikov, N. 2010, ApJ, 718, 488
Sidoli, L., Parmar, A. N., Oosterbroek, T., & Lumb, D. 2002, A&A, 385, 940
Sobczak, G. J., McClintock, J. E., Remillard, R. A., & Bailyn, C. D. 1999, ApJ, 520, 776
Sobczak, G. J., McClintock, J. E., Remillard, R. A., et al. 2000, ApJ, 544, 993
Soleri, P., Belloni, T., & Cassela, P. 2008, MNRAS, 383, 1089
Steiner, J. F., Narayan, R., McClintock, J. E., & Ebisawa, K. 2009, PASP, 121, 1279
Stiele, H., Belloni, T. M., Kalemci, E., & Motta, S. 2013, MNRAS, 429, 2655 (SBKM13)
Strohmayer, T. E., & Mushotzky, R. F. 2009, ApJ, 703, 1386
Sunyaev, R. A., Borozdin, K. N., Aleksandrovich, N. L., et al. 1994, AstL, 20, 777
Sunyaev, R. A., & Titarchuk, L. G. 1980, A&A, 86, 121
Tanaka, Y., & Lewin, W. H. G. 1995, in X-Ray Binaries, ed. W. H. G. Lewin, J. van Paradijs, & E. P. J. van den Heuvel (Cambridge: Cambridge Univ. Press), 126
Tanaka, Y., & Shibazaki, N. 1996, ARA&A, 34, 607
Titarchuk, L., Lapidus, I. I., & Muslimov, A. 1998, ApJ, 499, 315 (TLM98)
Titarchuk, L., & Osherovich, V. 1999, ApJL, 518, L95
Titarchuk, L., & Seifina, E. 2009, ApJ, 706, 1463 (TS09)
Titarchuk, L., & Shaposhnikov, N. 2010, ApJ, 724, 1147
Titarchuk, L., Shaposhnikov, N., & Arefiev, V. 2007, ApJ, 660, 556 (TSA07)
Titarchuk, L., & Zannias, T. 1998, ApJ, 493, 863
Tomsick, J. A., Corbel, S., Goldwurm, A., & Kaaret, Ph. 2005, ApJ, 630, 413 (T05)
Tomsick, J. A., & Kaaret, Ph. 2000, ApJ, 537, 448
Tomsick, J. A., Lapshov, I., & Kaaret, P. 1998, ApJ, 494, 747
Trudolyubov, S., Churazov, E., & Gilfanov, M. 1999, A&A, 351, L15
Trudolyubov, S., Gilfanov, M., Churazov, E., et al. 1998, A&A, 334, 895
Trudolyubov, S., Gilfanov, M. R., Churazov, E. M., et al. 1996, Astronomy Letters, 22, 664
Trudolyubov, S. P., Borozdin, K. N., & Priedhorsky, W. C. 2001, MNRAS, 322, 309
Ueda, Y., Inoue, H., Tanaka, Y., et al. 1998, ApJ, 492, 782
Ueda, Y., Murakami, H., Yamaoka, K., Donati, T., & Ebisawa, K. 2004, ApJ, 609, 325
Vignarca, F., Migliari, S., Belloni, T., Psaltis, D., & van der Klis, M. 2003, A&A, 397, 729
Wijnands, R., Homan, J., & van der Klis, M. 1999, ApJ, 526, L33
Yamaoka, K., Ueda, Y., Inoue, H., et al. 2001, PASJ, 53, 179